A Discrete Monolayer Cardiac Tissue Model for Tissue Preparation Specific Modeling

by

Jong M. Kim

Department of Biomedical Engineering
Duke University

Date:_______________________
Approved:

____
Craig Henriquez, Supervisor

____
Roger Barr

____
Nenad Bursac

____
John Trangenstein

____
Salim Idriss

Dissertation submitted in partial fulfillment of
the requirements for the degree of
Doctor of Philosophy in the Department of
Biomedical Engineering in the Graduate School
of Duke University

2010

ABSTRACT

A Discrete Monolayer Cardiac Tissue Model for Tissue Preparation Specific Modeling

by

Jong M. Kim

Department of Biomedical Engineering
Duke University

Date:_______________________
Approved:

____
Craig Henriquez, Supervisor

____
Roger Barr

____
Nenad Bursac

____
John Trangenstein

____
Salim Idriss

An abstract of a dissertation submitted in partial
fulfillment of the requirements for the degree of
Doctor of Philosophy in the Department of
Biomedical Engineering in the Graduate School
of Duke University

2010

Abstract

Engineered monolayers created by using microabrasion and micropatterning methods have provided a simplified *in vitro* system to study the effects of anisotropy and fiber direction on electrical propagation. Interpreting the behavior in these culture systems has often been performed using classical computer models with continuous properties. Such models, however, do not account for the effects of random cell shapes, cell orientations and cleft spaces inherent in these monolayers on the resulting wavefront conduction. Additionally when the continuous computer model is built to study impulse propagations, the intracellular conductivities of the model are commonly assigned to match impulse conduction velocity of the model to the experimental measurement. However this method can result in inaccurate intracellular conductivities considering the relationship among the conduction velocity, intracellular conductivities and ion channel properties. In this study, we present novel methods for modeling a monolayer cardiac tissue and for estimating intracellular conductivities from an optical mapping. First, in the proposed method for modeling a monolayer of cardiac tissue, the factors governing cell shape, cell-to-cell coupling and the degree of cleft space are not constant but rather are treated as spatially random with assigned distributions. This approach makes it possible to simulate wavefront propagation in a manner analogous to performing experiments on engineered monolayer tissues. Simulated results are compared to reported experimental data measured from monolayers used to investigate the role of cellular architecture on conduction velocities and anisotropy ratios. We also present an estimate for obtaining the electrical properties from these networks and demonstrate how variations in the discrete cellular architecture affect the macroscopic conductivities. The simulation results agree with the common assumption that under normal ranges of coupling strengths, tissues whose cell shapes and connectivity show relatively uniform distributions can be represented using continuous models with conductivities derived from random discrete cellular architecture using the estimates. The results also reveal that in the presence of abrupt changes in cell orientation, local estimates of tissue properties predict smoother changes in conductivities that may not adequately predict the discrete nature of propagation at the transition sites. Second, a novel approach is proposed to estimate intracellular conductivities from the optical mapping of the monolayer cardiac tissue under subthreshold stimulus. This method uses a simplified membrane model, which represents the membrane as a second order polynomial of the membrane potential. The simplified membrane model and the intracellular conductivities are estimated from the signals similar to that would be obtained from the optical mapping of the monolayer tissue under the subthreshold stimulus. We showed that the proposed method provides more accurate intracellular conductivities compared to a method using a constant membrane resistance.

Dedication

For my wife, Jeongmin and son, Alexander Hyunsoo

Contents

List of Tables

List of Figures

1. Introduction

1.1 Discrete action potential (AP) conduction in cardiac tissue

Cardiac cells are electrically coupled with gap junctions enabling action potentials to propagate through cardiac tissue. In early investigations of action potential (AP) conduction, the tissue was assumed to be a continuous medium due to the tight coupling by gap junctions and the relatively smooth patterns of activation (Roberge, Vinet et al. 1986; Plonsey and Barr 1987; Muzikant, Hsu et al. 2002). In the early 1980's, Spach et al. reported observations from their experiments that were contradictory to the continuous model's predictions (Spach, Miller et al. 1981). Their findings and an increased emphasis on a gap junction function led to more computer models incorporating discrete and heterogeneous features of cardiac tissue. In continuous media, AP propagation can be described by the continuous cable model, which determines the relationship between the transmembrane potential and ionic transmembrane current in one dimensional fiber.

$$C_m \cdot \frac{\partial V}{\partial t} + I_{ion} = \frac{a}{2 \cdot R_i} \cdot \frac{\partial^2 V}{\partial x^2} \tag{1.1}$$

where a is a radius of the fiber, R_i is intracellular resitivity (Ωcm) and C_m is the specific membrane capacitance ($\mu F/cm^2$). From equation (1.1), the approximate impulse conduction velocity (CV) θ can be obtained with sodium conductance and intracellular resistance (Pickard 1966).

$$\theta = \frac{4}{3}\left(\frac{2a^2 \cdot \Upsilon_0}{C_m^3 \cdot R_i^2}\left(\frac{V_T}{2\psi_0 - V_T}\right)^3\right)^{1/4} \tag{1.2}$$

where Υ_0 is average maximum rate of rise of the sodium conductance per unit area, ψ_0 is resting potential, and V_T is threshold potential. The equation (1.2) provides two mechanisms for conduction velocity changes. The first one is through changes in the sodium current, which is due to positive correlation between θ and Υ_0. This mechanism can be experimentally detected by the changes in the waveforms and the maximum upstroke velocity since both are correlated to the conductance of the sodium channel during action potential upstroke. The other mechanism involves the change in intracellular resitivity R_i, which is inversely proportional to the CV. If the velocity changes by the second mechanism, the continuous model predicts that the waveform does not change since the intracellular resistance and the sodium channel conductance are independent.

When Spach et al. measured AP upstroke velocity and CV at one site of canine cardiac muscle, the result could not be explained with continuous view of AP conduction (Spach, Miller et al. 1981). The investigators placed one recording electrode and 2-6 stimulus electrodes around the recording site so that they could record AP propagating in different directions at one recording site. Under this condition, the investigators observed that the longitudinal conduction velocity (LCV) was faster than transverse conduction velocity (TCV) with the ratio of 2.6 and the velocity change was associated with the waveform change. Longitudinal propagation was associated with smooth waveform but transverse propagation was associated with non-smooth waveforms, which supports CV change due to sodium channel conductance. However, the maximum upstroke velocity was higher during the transverse propagation than during the longitudinal propagation. These results were inconsistent with the mechanisms of the conduction velocity change from the continuous model, predicting the positive correlation between CV and upstroke velocity $\dot{V}_{max}$ or no change in the waveform depending on the mechanisms of the velocity change.

1.2 Cultured monolayer cardiac tissue

Recent advances in tissue engineering and micropatterning techniques have made it possible to create monolayers in which the degree of anisotropy can be reproducibly controlled (Fast and Kleber 1994; Bursac, Parker et al. 2002; Rohr, Fluckiger-Labrada et al. 2003; Bian and Tung 2006). Bursac et al. presented an *in vitro* model system that enables systematic manipulation of the degree, orientation, and nonuniformity (continuity) of anisotropy in centimeter-sized monolayer cultures of neonatal rat cardiac myocytes (Bursac, Parker et al. 2002). Using micropatterning, they cultured a series of cardiac monolayer tissues whose microscale continuity changes from discontinuous to continuous and the cell orientations change from oriented (anisotropic) to disoriented (isotropic). While these experimental monolayers allow for sophisticated electrophysiological, pharmacological, and genetic studies of simple impulse propagation and reentry dynamics *in vitro*, they are currently limited to rat neonatal cells with electrophysiological properties that differ from humans. In addition, some features of the tissue, like the magnitude and distribution of gap junctions, are not easy to control locally.

Another benefit of using an *in vitro* monolayer of cardiac tissue is that impulse conduction can be observed over wide area of the tissue with an optical mapping which uses voltage sensitive dyes in the cardiac tissue so that the fluorescence can be related to the transmembrane potential (Entcheva, Lu et al. 2000). The fluoresced light is captured with video imaging device or optical sensors whose signal gives relative values of potential rather than absolute values (Gray 1999). This method allows the ability to observe impulse conduction with very high spatial resolutions by magnifying the tissue with microscopes. In addition, the optical mapping from the monolayer tissue can be directly compared with a computer model, which allows additional analysis and testing of hypotheses (Entcheva, Lu et al. 2000).

1.3 Computer models of discrete myocardium

In computational electrophysiology, a monolayer (2D) cardiac tissue model has been an efficient tool for studying AP conduction properties when it is compared to a one dimensional fiber or to three dimensional tissues. In a one dimensional fiber, cells are connected only by end-to-end and it is difficult to represent certain types of heterogeneity observed in cardiac tissue. In a three dimensional network, the increased dimensions of the domain does not only increase the computational complexity significantly, but also presents challenges in visualizing and analyzing the data. However, in two dimensions, the heterogeneity of the tissue can be incorporated into the model and properties of impulse conduction can be easily compared to those of tissue slices and engineered monolayers. The 2D models can be simulated much more efficiently than in 3D.

Early cardiac tissue models were extended from the core conductor model under the assumption that the cardiac tissue can be approximated as a continuous medium. In such a continuous cardiac model, gap junctions and cell shapes were considered to affect impulse conduction only through their effects on average electrical properties.

In light of Spach et al.'s findings (Spach, Miller et al. 1981), cardiac tissue models began to emerge that included discrete cells connected with high resistance gap junctions. Leon and Roberge modeled a thin sheet of cardiac tissue with parallel excitable cables connected with regular array of identical resistors (Leon and Roberge 1991). This model was computationally very efficient but it did not represent longitudinal discontinuity. Fast and Kleber extended the parallel cable model by introducing gap junctions in longitudinal direction (Fast and Kleber 1993). The authors estimated intracellular conductivity and gap junction conductance for this tissue model by matching CV and properties of impulse conduction measured in one dimensional fiber and a corresponding fiber model. Although this model clearly defined cell boundaries with gap resistance higher than intracellular resistance, the shapes of cells were identical and gap junctions were regularly distributed with an identical value. In order to build a more realistic monolayer tissue model, Spach et al. duplicated cell boundaries from cell isolations and arranged gap junctions similar to that observed in native tissue (Spach and Heidlage 1995). For model parameters, the authors either used experimentally measured values or chose values so that the resulting simulated behavior was consistent with experimental observations. With this model, they observed complicated patterns of CV and upstroke velocity due to the cell architecture. Although this model was carefully built to produce consistent results compared to those of tissue slice, there were still structural limitations; the boundaries of cells were stair stepped and the orientations of cells were parallel or orthogonal to each other. This cell shape might be proper for adult cells but not for neonatal cells which have a more spindle-like shape. Moreover, regarding the orientation of cells, more variations and complexities are observed at branch sites and particularly in cultured tissues. The structural components of the cardiac models have been developed to include more heterogeneous features of the tissue as the experimental findings indicate the importance of them. Despite such developments, the existing models still have restrictions on shapes and orientations of cells and there is no efficient method to estimate intracellular conductivity and gap junction properties for the tissue models. In addition to these modeling efforts, Fast and

Kleber estimated intracellular conductivity and gap junction strength of a tissue fiber by matching the conduction velocity and other observations (Fast and Kleber 1993). Although it seems feasible to estimate intracellular conductivity and gap junction conductance in a two dimensional tissue with optical mapping by modifying the work of Fast and Kleber in one dimensional fiber (Fast and Kleber 1993), the increased dimensionality makes this complicated.

1.4 Model parameter estimation

Regardless of the type of the computer model, the model requires parameters that can be estimated from a set of experimental measurements. These parameters describe the passive electrical properties of the tissue but have different physical meanings depending on the model. In the bidomain model where the tissue is homogenized with the extracellular space, the parameters are effective intracellular and extracellular conductivities, which represent averaged electrical properties. Due to the averaging, each of these parameters can be represented with three values or one value for each direction in the three dimensional space. On the other hand, the monodomain model assumes that the extracellular conductivity is infinite and the method can vary depending on the way cells and tissues are represented. If the monodomain model is implemented with a continuous medium, this implementation only requires intracellular conductivities, which can be considered as averaged electrical properties of the tissue. In the other implementation, the tissue can be represented as collection of discrete cells connected by gap junctions. This implementation requires a lot more information on the tissue including intracellular conductivities, gap coupling strength, cell shapes, and distribution of clefts.

Many of the bidomain parameter estimation methods are based on the four-electrode technique and its variations. The four-electrode technique uses a linear array of four equally spaced electrodes. The outer two electrodes deliver an applied current, while the inner two electrodes measure the resulting voltage (Plonsey and Barr 1982). Plonsey and Barr showed that this method could be used for estimating bidomain parameters when the domain has an equal anisotropy ratio (i.e., the anisotropy of the intracellular and extracellular domains have the same ratio). This method has been extended to eliminate the equal anisotropy ratio condition and to handle the alignment between the fiber and the electrode by using multiple electrodes or high frequency stimulus with a numerical method for data fitting (Le Guyader, Trelles et al. 2001; Pollard and Barr 2006; Sadleir and Henriquez 2006).

While the bidomain model parameter estimation has been studied to use advanced numerical methods, there are almost no studies estimating monodomain model parameters. This is probably because matching CV is usually considered sufficient for homogeneous tissue models. However this method is possible only when the membrane dynamics are correctly modeled and in many cases membrane dynamics of the neonatal cells used *in vitro* system is not well described. Although there is few study for which estimating monodomain parameter was the main goal (van Oosterom, de Boer et al. 1979; Plonsey and Barr 1986), Fast and Kleber used optical mapping data to estimate the intracellular conductivity and gap junction conductance for one dimensional discrete fiber model (Fast and Kleber 1993).

1.5 Objectives and Organization

Building a computer model to simulate a natural system always involves simplifications, because either the natural system is too complicated or has too many immeasurable model parameters. For cardiac tissue, the microscopic heterogeneity has been assumed to have minimal effects on impulse conduction because of the complexity of the model and the difficulties in measuring model parameters.

There is growing experimental evidence that indicate that the microscopic heterogeneity of the tissue is important for the mechanisms of arrhythmias (Spach and Boineau 1997; Kanno and Saffitz 2001; Zlochiver, Munoz et al. 2008). However there are numerous technical challenges in experimental methods to study fully the role of microscopic heterogeneity of the tissue in the mechanisms of arrhythmias. Computational tools can alleviate such limitations by allowing fine control on the experimental condition and by providing some insight into the internal ionic channel dynamics that are not measurable in the tissue.

In this thesis, we developed computational tools to model a monolayer cardiac tissue. The method assumes that the factors governing cell shape, cell-to-cell coupling and the degree of cleft space are not constant but rather are spatially random with assigned distributions. Using this approach, we have conducted a simulation study on the role of cellular architecture on conduction velocities and anisotropy ratio. Because of the need to better understand how the discrete cellular structure impacts current flow, we have also developed methods to estimate the effective intracellular conductivities using data that can be derived from the optical mapping experiments.

Chapter 2 presents the derivation of finite element method (FEM) based monodomain model to simulate monolayer tissues. This method was derived from a complete three dimensional FEM describing a monolayer tissue. The three dimensional FEM can model arbitrarily shaped cells but has the obvious disadvantage of requiring more computational resources than two dimensional finite difference or finite volume method. This disadvantage was resolved by applying algebraic reduction of FEM in depth direction of the tissue. This reduction can lead to numerical errors due to the loss of dimensionality. Numerical tests were performed that showed that the algebraic reduction did not cause significant numerical error.

Chapter 3 presents an in depth simulation study investigating the role of the orientations and size of cell, and distributions of clefts on the conduction velocities and anisotropy ratio. In order to make it possible to simulate impulse conduction through tissues with varying discrete properties, a discrete tissue generator was developed. This tissue generator can generate a tissue in which shapes and orientations of cells and distribution of clefts can be controlled to follow spatial random distribution. This tissue generation method made it possible to perform simulations similar to experimental settings. Tissues with various alignments of cells and distributions of clefts were generated and then the relationship between these discrete features of the tissue and impulse conduction velocity was studied. The simulation results were compared to published experimental results and it showed a good agreement. This chapter was recently accepted for publication by the Biophysical Journal (Kim, Bursac et al. 2010).

Chapter 4 presents an improved method for estimating the intracellular conductivities from the optical mapping. To improve the accuracy of the estimation, this method uses a simplified membrane model that describes membrane resistance under the subthreshold stimulus as a second order polynomial of membrane potential.

Chapter 5 discusses the general conclusions as well as the limitations, applications and suggestions for the future study.

2. Finite element method based monodomain model for monolayer tissue simulation

While many models have used to simulate action potential propagation in a cardiac monolayer tissue, all have been assumed that the tissue is either continuous or discrete with a regular cell structure coupled through gap junctions. There are several experimental and computational studies that indicate that conduction velocity (CV) and upstroke velocity $\dot{V}_{max}$ are determined by microscopic heterogeneity such as sizes and orientations of cells; and distributions and values of gap junctions (Spach, Miller et al. 1981; Spach and Heidlage 1995; Kanno and Saffitz 2001; Hubbard, Ying et al. 2007; Jacquemet and Henriquez 2008) that are not captured by these traditional models. Currently available discrete computational models for a monolayer tissue were derived from a finite difference method (FDM) or a finite volume method (FVM). Because of their simplicity, domains are often discretized as Cartesian grids although this leads to highly idealized geometries. While FVM and FEM can be performed on non-Cartesian grids, a more robust approach to handle more complex domains is the Finite Element Method (FEM). The FEM provides a natural framework that can mimic ionic current, capacitive current and gap junctional current in the model.

In this chapter, an efficient numerical model to handle a tissue with arbitrary shaped cells was developed by reducing a three dimensional FEM into a two dimensional FEM under two conditions: symmetry of the tissue in the depth direction and the use of a single element to discretize the depth direction. The resulting two dimensional model can simulate a monolayer tissue with arbitrary cell geometry and gap junction distributions with very good accuracy (compared to the full three dimensional mode) with significantly less memory requirements and with much greater computational efficiency.

2.1 Introduction

To study action potential (AP) propagation, cardiac tissue has been usually considered as continuous, uniform, and homogeneous medium (Roberge, Vinet et al. 1986; Plonsey and Barr 1987; Muzikant, Hsu et al. 2002). However, recent experimental evidences indicate that AP propagation only appears as continuous in macro scale but at the micro scale, it is discrete (Spach, Miller et al. 1981; Spach and Heidlage 1995). The discreteness arises, in part, from the variation in the size and shape of cells, the gap junction locations, and distributions of clefts (Spach, Miller et al. 1981; Bursac, Parker et al. 2002). This discreteness is enhanced as a result of aging or disease by a redistribution of gap junctions and development of micro fibrosis (Ausma, Wijffels et al. 1997; Everett, Li et al. 2000; Kostin, Klein et al. 2002; Spach, Heidlage et al. 2007). The increased micro-heterogeneity has been associated with change of CV and AP upstroke velocity (Spach and Dolber 1986; Spach, Dolber et al. 1988; Koura, Hara et al. 2002). These findings suggested that, with changes of membrane ionic channels, the changes of the tissue heterogeneity are important for the initiation, maintenance, and termination of reentrant arrhythmias, which cause irregular heartbeats (Spach, Miller et al. 1981; Spach and Dolber 1986; Spach, Dolber et al. 1988; Spach and Boineau 1997). Despite such electrophysiological implication for arrhythmias, the interactions between microstructure of tissue and dynamics of reentrance are not well understood due to lack of experimental and computational tools (Spach and Heidlage 1995).

In studying AP propagation at a cardiac tissue, experiments and computer models are complementary. Many studies have been performed that combine experiments and computer simulations (Fast and Kleber 1993; Fast and Kleber 1995; Spach, Heidlage et al. 2000; Sharma and Tung 2001). In most cases, the computer models were built from experimental observations so that the model could be consistent with the experimental conditions. This kind of computer model can provide information unavailable under experimental conditions such as the dynamics of individual ion currents or ion channel conductances (Spach and Heidlage 1995; Henriquez, Muzikant et al. 1996; Shaw and Rudy 1997). Moreover the model can be used to test a hypothesis since the model parameters can be changed separately, which is not always possible in an experiment (Shaw and Rudy 1997; Spach, Heidlage et al. 2000; Spach, Heidlage et al. 2004). However typical computer models tend to simplify the heterogeneous structure of the target tissue, assuming it to be continuous or composed of regularly structured cells. High levels of heterogeneity in a tissue can be caused by aging or disease; or can be intentionally created through directed cell growth in cultured cardiac tissues (Spach and

Dolber 1986; Spach, Dolber et al. 1988; Bursac, Parker et al. 2002; Koura, Hara et al. 2002). If a heterogeneous tissue is modeled as continuous or with simple cell structures, it might not be able to capture the effects of known features of heterogeneity such as shape and size of cells and distributions of clefts.

In this study, we formulated a two dimensional tissue monolayer model by reducing a dimension of a three dimensional FEM model so that a monolayer tissue with arbitrary cell shape can be efficiently simulated. In order to do this, symmetry was assumed in the depth direction and the depth was discretized using only one element. This reduction is expected to cause some error. First, the restriction on the discretization assumes that the intracellular potential in depth direction is near constant. If this assumption is not met, it can affect significantly CV and $\dot{V}_{max}$. Second, when the distributions of gap junctions in three dimensions are reduced into two dimensions, there are an infinite number of three dimensional distributions of gap junctions which will appear identical in two dimensions. Some of distributions can increase the nonlinearity of intracellular potential in the depth. The effect of the reduction was numerically tested by comparing a two dimensional model and a three dimensional model with fine depth discretization and various distributions of gap junctions.

2.2 Methods

2.2.1 Three dimensional model formulation

Three dimensional model formulations used in this study closely follows the FEM formulation by Ying and Henriquez (Ying and Henriquez 2007). Cardiac tissue can be viewed as a network of cells electrically coupled through gap junctions. In two dimensions (i.e. a tissue monolayer), each cell can be simplified as a unit with uniform thickness Δz whose boundary Γ is defined by a membrane with the interior Ω_i and the exterior Ω_e. The potential inside and outside the cell satisfies Laplace's equation, namely

$$\nabla \cdot \sigma_i \nabla \phi_i = 0 \quad in \quad \Omega_\mathrm{i} \tag{2.1}$$

$$\nabla \cdot \sigma_e \nabla \phi_e = 0 \quad in \quad \Omega_\mathrm{e} \tag{2.2}$$

where ϕ_i is intracellular potential (mV), ϕ_e is extracellular potential , σ_i is intracellular conductivity tensor (mS/cm) and σ_e is extracellular conductivity tensor. The transmembrane potential V and transmembrane current density I_m are defined at the membrane of each cell Γ from intracellular and extracellular potential.

$$\phi_i - \phi_e = V \tag{2.3}$$

$$n \cdot \sigma_i \nabla \phi_i = I_m \tag{2.4}$$

$$n \cdot \sigma_e \nabla \phi_e = -I_m \tag{2.5}$$

n is a unit vector normal to the boundary. The transmembrane current density I_m is sum of capacitive current density I_{cap} , ionic current density I_{ion} , and gap junctional current density I_{gap}, each of which is a function of transmembrane potential or intracellular potential.

$$I_m = I_{ion} + I_{cap} + I_{gap} \tag{2.6}$$

$$I_{cap} = C_m \frac{dV}{dt} \tag{2.7}$$

$$I_{ion} = \mathcal{F}(V, q) \tag{2.8}$$

$$I_{gap} = \sigma_g (\phi_{i,a} - \phi_{i,b}) \tag{2.9}$$

C_m is the specific membrane capacitance ($\mu F/cm^2$) and σ_g is the gap junction conductance (mS/cm^2). $\phi_{i,a}$ and $\phi_{i,b}$ are the intracellular potential of the nodes coupled by the gap junction i between cell a and b. $\mathcal{F}$ of I_{ion} is a function defining the membrane dynamics and is usually a nonlinear function of the transmembrane potential and state variables, q.

For a tissue in a large bath, the problem can be simplified by assuming infinite extracellular conductivity and zero extracellular potential such that $\phi_i = V$. This condition enables us to rewrite the problem in the following form:

$$\nabla \cdot \sigma_i \nabla V = 0 \quad in \quad \Omega_\mathrm{i} \tag{2.10}$$

$$n \cdot \sigma_i \nabla V = I_m \quad on \quad \Gamma \tag{2.11}$$

This PDE can be solved numerically using a technique such as the finite volume method (FVM) or the finite element method (FEM). Using the FVM on a structured grid, the resulting system can be considered as a network of resistors similar to the approach used by Spach et al. (Spach and Heidlage 1995; Rose, Shao et al. 2000). FEM with unstructured grids can model arbitrary shaped cells. However, with FEM, three dimensional structure is assumed and the resultant linear system is significant larger than that of FVM.

2.2.2 Reduction to the two dimensional model

In this section, the three dimensional model from the previous section is algebraically reduced to the two dimensional model. With a simplified cell in Figure 2.1, it is assumed that the cell geometry and the boundary conditions are symmetric in the depth direction. With proper shape functions in FEM, the intracellular potential ϕ_i can be decomposed into ϕ_{top} and ϕ_{bottom} such that ϕ_{top} vanishes on Γ_{bottom} and ϕ_{bottom} vanishes on Γ_{top}. In addition to this, the symmetry condition makes ϕ_{top} and ϕ_{bottom} symmetric in the depth direction.

$$\phi_i = \phi_{top} + \phi_{bottom} \tag{2.12}$$

$$\phi_{top} = 0 \quad on \quad \Gamma_{bottom} \tag{2.13}$$

$$\phi_{bottom} = 0 \quad on \quad \Gamma_{top} \tag{2.14}$$

$$\phi_{bottom}(z) = \phi_{top}(-z) \tag{2.15}$$

In a similar manner, the membrane current I_m can be decomposed with symmetric shape functions: $I_{m,top}$ and $I_{m,bottom}$.

$$I_m = I_{m,top} + I_{m,bottom} \tag{2.16}$$

$$I_{m,top} = 0 \quad on \quad \Gamma_{bottom} \tag{2.17}$$

$$I_{m,bottom} = 0 \quad on \quad \Gamma_{top} \tag{2.18}$$

$$I_{m,bottom}(z) = -I_{m,top}(-z) \tag{2.19}$$

Note that ϕ_{top} and ϕ_{bottom} have the same polarity in equation (2.15) but it is inverted in $I_{m,top}$ and $I_{m,bottom}$ of equation (2.19). This is because the transmembrane currents have the same amplitude on Γ_{top} and Γ_{bottom} but they flow in opposite directions. From these symmetric shape function decompositions, the each side of the equation (2.4) becomes the following.

$$\begin{aligned} n \cdot \sigma_i \nabla \phi_i &= n \cdot \sigma_i \nabla \left(\phi_{top}(z) + \phi_{bottom}(z) \right) \\ &= n \cdot \sigma_i \nabla \left(\phi_{top}(z) + \phi_{top}(-z) \right) \end{aligned} \tag{2.20}$$

$$\begin{aligned} I_m &= I_{m,top}(z) + I_{m,bottom}(z) \\ &= I_{m,top}(z) - I_{m,top\,(-z)} \end{aligned} \tag{2.21}$$

In solving equations (2.1), (2.4), (2.20), and (2.21) with FEM, the domain in Figure 2.1 can be discretized with one element in the depth direction and thus the three dimensional PDE problem effectively becomes two dimensional problem because equation (2.20) and (2.21) enable the intracellular potential and the membrane current to be obtained by solving the PDE only on the either side of the membrane.

In contrast to the continuous tissue model, the discrete tissue mode consists of individual cells electrically coupled through gap junctions. While the continuous tissue can be considered as a two dimensional structure, an individual cell in the discrete tissue model has three-dimensional structure and currents can flow through the lateral face. If the ionic current flow through lateral face is allowed, there will be large discrepancy in the surface area of the tissue between the continuous model and the discrete model. To avoid such a discrepancy, the ionic and capacitive currents were blocked and only gap junctional current was allowed. More detailed information on numerical implementation can be found in Appendix A.

Note that in contrast to classical monodomain formulations, a surface-to-volume ratio is not used. The surface-to-volume ratio can be used to compensate for the difference between the geometric membrane surface area and the actual membrane surface area arising from membrane folding. While the geometric surface area was assumed in this study, folding can be incorporated by appropriately scaling I_{cap} and I_{ion} in equation (2.6).

The reduction from a three dimensional formulation to the two dimensional formulation restricts the boundary condition to be symmetric in depth direction and the depth discretization of the tissue is represented by one element. The restriction on the depth direction discretization can result in numerical error if the intracellular potential has a large nonlinearity in depth direction. To investigate the effect of a single element in the depth direction, numerical results were obtained with finer depth direction discretization for comparison.

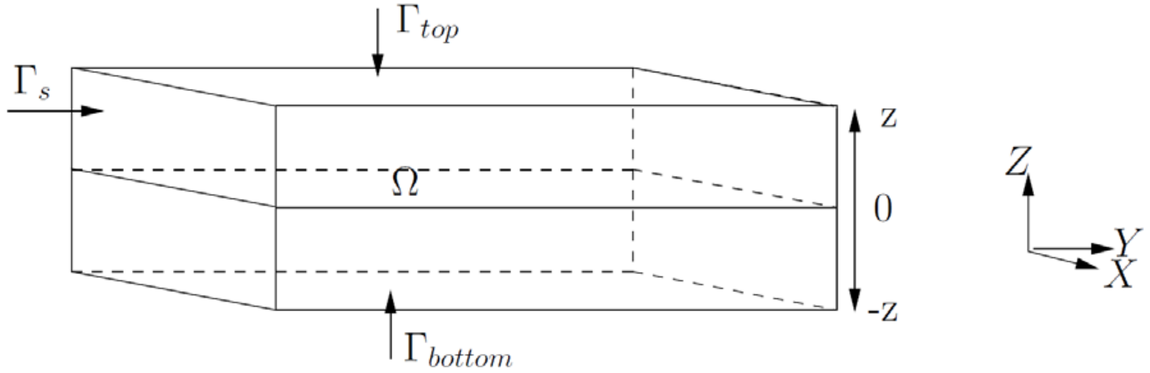

Figure 2.1: A cell is symmetric in the depth (z) direction. Γ_{top} and Γ_{bottom} are top and bottom membrane, respectively. The line dividing the cell is a plane of symmetry

2.2.3 Tissue structure

In our study, three tissue structures were simulated: uniform brick (UN), brick wall (BW) and random tissue (RT). The UN and BW were from Hubbard et al. (Hubbard, Ying et al. 2007) and RT was built based on a stained image (Figure 2.2). Following Hubbard et al., UN and BW consist of uniform brick cells of 144 μm in length and 24 μm in width. As shown in Figure 2.2, UN has cells stacked directly on top of each other and BW has cells overlapped similar to a brick wall. RT model was hand drawn from an image of stained tissue to build a more realistic tissue model with cells of varying shapes and orientations. For all cases, the cell thickness was assumed to be 11.3 μm and the intracellular conductivity was 4 mS/cm. For the given tissue structure, gap junctions were assigned on boundary edges to mimic those of neonatal cells. In UN and BW model, the gap junctions were assigned every 8 μm around cells and, in RT model, they were assigned if the distance between edges from neighboring cells were close enough. As a result of this, UN and BW tissue had 42 junctions per cell and RT tissue had average 22 gap junctions per cell.

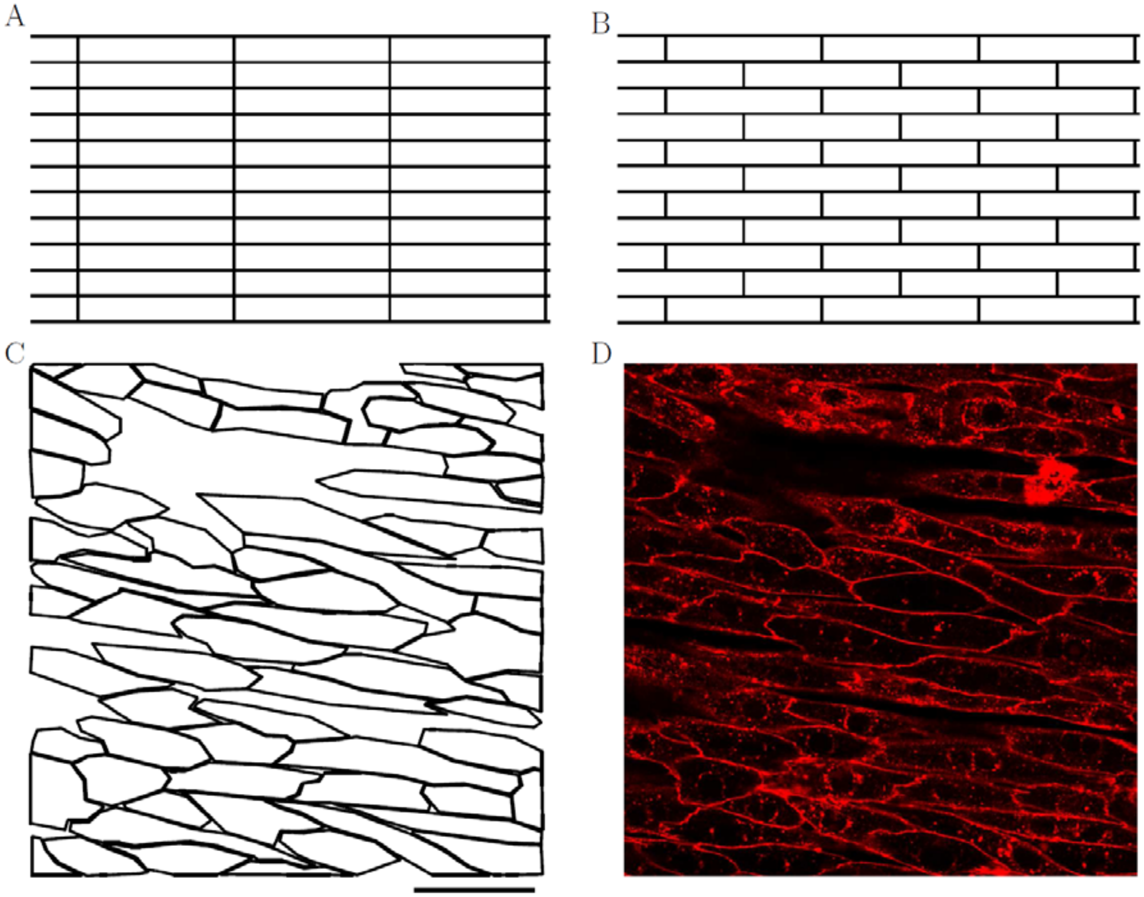

Figure 2.2: UN, BW and RT cell boundaries in the tissue model and stained tissue image used for RT. While UN and BW have regular tissue structure, RT is hand-drawn from stained tissue image and has irregular structure. The scale bar under the RT is 100 μm.

2.2.4 Discretization

In order to simulate AP propagation in these tissues, cells were separately discretized. The UN and BW models were discretized by right isosceles triangles with a cathetus of length 8 μm and the RT model was discretized with triangle area smaller than 25 μm^2 (Figure 2.3) using the software package, Triangle (Shewchuk 2002). Three dimensional tissue models were also built in order to test the effects of depth discretization due to the nonlinearity of intracellular potential in that direction. For three dimensional model discretizations, the two dimensional discretizations were extended to three dimensional ones by imagining the triangles as projections of prism elements as shown in Figure 2.3. The three dimensional models were discretized into nine elements in depth direction so that the nonlinearity in the depth direction can be solved properly.

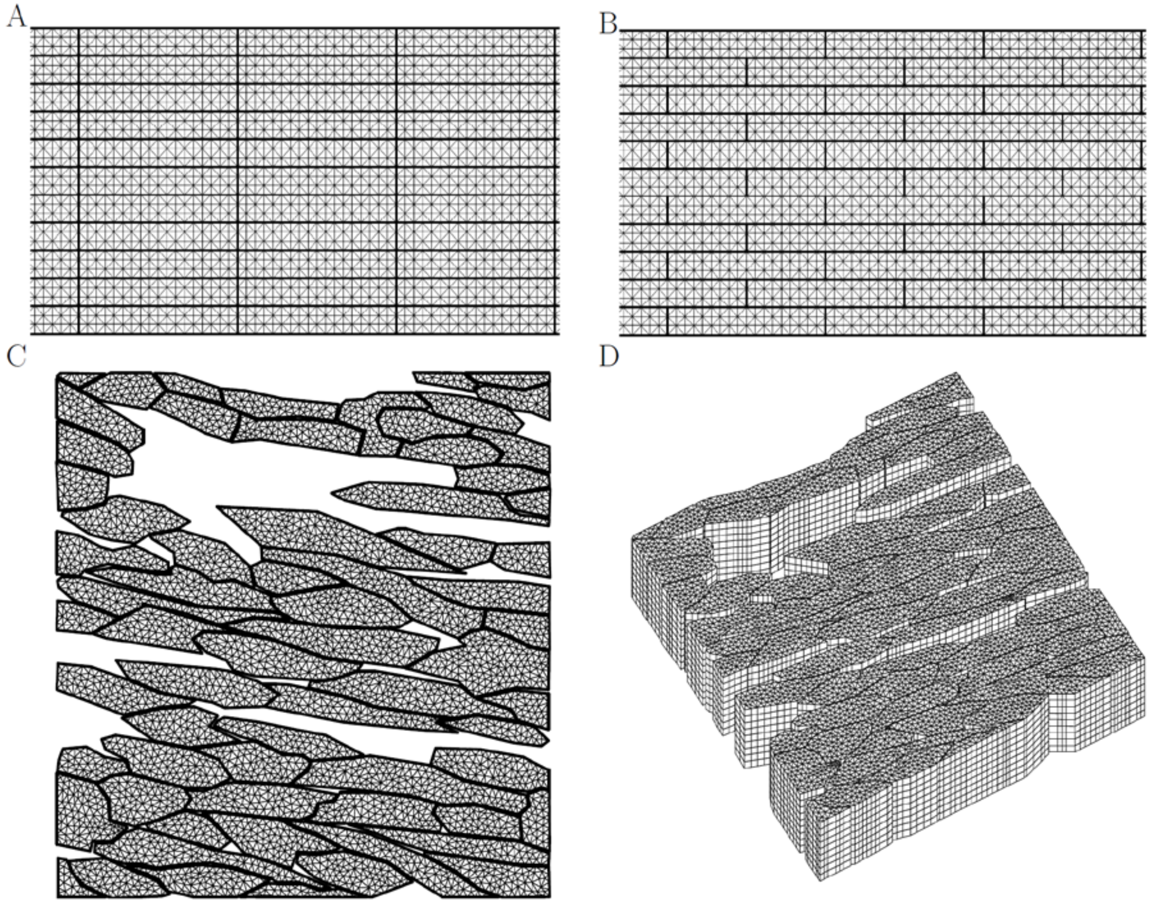

Figure 2.3: two and three dimensional discretization of tissues. UN and BW were discretized with structured grids. RT was discretized with unstructured grids because of the irregular shapes of cells. These two dimensional discretizations were extended to three dimensional discretizations by imagining triangles as projection of prism elements. The triangulation of RT was done with Triangle (Shewchuk 2002).

2.2.5 Node coupling for gap junction

The gap junctions between cells were implemented by coupling the potential and the current of the nodes where the gap junctions were located. This coupling is trivial with uniform or brick shaped cells where nodes between two adjacent cells are well aligned and the coupling these nodes is straightforward. With randomly shaped cells, however, coupling nodes to implement gap junctions is not trivial, because the nodes between two adjacent cells are not necessarily aligned. When a discrete tissue pattern was provided for the simulation, every pair of cells in this tissue was tested to determine the neighbors. For each neighboring pair of cells, the cell-to-cell contact segment was defined as the cell boundary segment whose distance was closer than 1 μm between the adjacent cells. The gap junction was assumed to exist uniformly on the cell-to-cell contact segment and the potential at the gap junction for the equation (2.9) was obtained by linear interpolation of the transmembrane potential from the nearest FEM nodes.

As shown in Figure 2.4, in the two dimensional model, the coupling was made on boundary edges covering gap junctions. In a similar manner, the three dimensional model coupling was made on the boundary faces covering gap junctions but the distributions of gap junctions in the three dimensional model are not equivalent to those of two dimensional model even though the same number of connections exist between cells. While the gap junctions distribute on one dimensional edges in the two dimensional model, the gap junctions distribute on two dimensional faces in the three dimensional model. This difference in dimensions leads to the situation where several different gap junction distributions in three dimensional models appear identical in the two dimensional models. For example, the gap junctions in Figure 2.4 B, C, and D vary in the distribution but, when they are modeled in two dimensions, they appear identical as they distribute uniformly in length and width direction. To test the effects of gap junction distributions we tested three gap junction distributions in the three dimensional model: uniform (3DU), concentrated (3DC) and random (3DR). 3DU model has the gap junctions uniformly distributed over the lateral membrane (Figure 2.4 B) and 3DC model has the gap junctions located at the center of lateral membrane in depth direction (Figure 2.4 C). These two models do not violate the symmetry condition and their gap junction distributions in two dimensional projection are identical. In 3DR model, although its gap junction distribution in two dimensional projection still looks same as those of other models, the gap junctions are randomly located on the lateral membrane (Figure 2.4 D). This model can test the effects when the depth directional symmetry condition is violated in gap junction distributions.

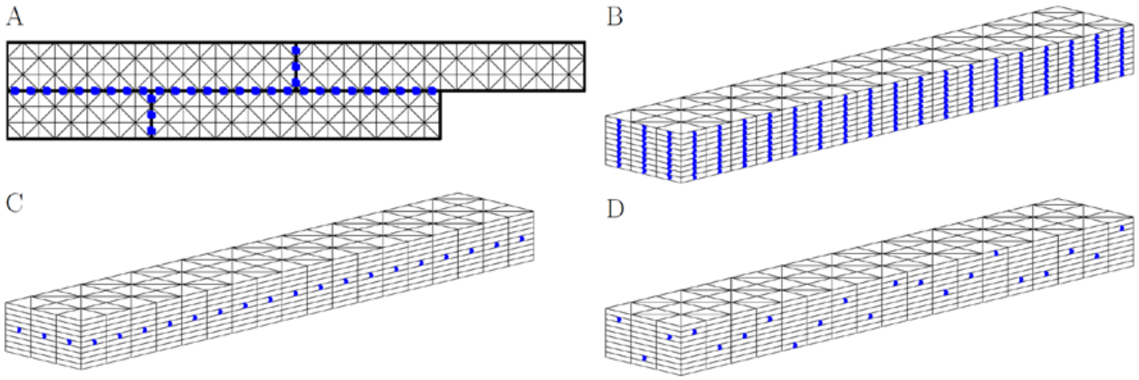

Figure 2.4: In two dimensional and three dimensional cell models, gap junctions appear as dots on the boundary of cells. The two dimensional model has gap junctions on the boundary edges (A) and the three dimensional models have gap junctions on the boundary face (B, C, and D). When the three dimensional models are reduced to the two dimensional model, different distributions of gap junctions in B, C, and D become indistinguishable in the two dimensional model.

2.2.6 Membrane dynamics

Luo-Rudy membrane model was used for membrane dynamics with modified calcium kinetics (Luo and Rudy 1991; Hubbard, Ying et al. 2007). This modification scaled up the calcium current by factor 4 but did not change the sodium current during upstroke in well coupled tissue. However, in low gap junction conductivity condition, this modification increased CV by increasing slow calcium currents.

2.2.7 Computation

In order to build a linear system for solving equation (2.1), from these two dimensional and three dimensional discretizations, FEM was used for the diffusion step and Crank-Nicolson with time step size 2.5 μsec was used for the reaction step (Keener and Bogar 1998). The resultant linear system was iteratively solved by BiCGSTAB with SSOR preconditioner (Vandervorst 1992) due to the non-symmetric linear system.

2.3 Results

The two dimensional FEM model was numerically tested by comparing with the two dimensional FDM model and the three dimensional FEM models. The two dimensional FDM model's results were from the study by Hubbard et al. which simulated effects of the gap junction distribution on AP propagation (Hubbard, Ying et al. 2007). Among their various cases, we reproduced their results in the two simplest tissue structures (UN and BW). In the comparison with three dimensional models (3DU, 3DC and 3DR), the effects of the depth discretization and the gap junction distribution were tested.

2.3.1 Comparison to the two dimensional FDM model

In order to match Hubbard et al.'s implementation, our model was modified. First, as with Hubbard et al., the lateral membrane was assumed to not conduct current. To mimic the surface-to-volume ratio used in their model, the membrane area was scaled by the factor 1.89.

After AP was initiated by stimulating the left boundary of the tissues for 1 $msec$, the CV and $\dot{V}_{max}$ were measured at the center of the tissue. According to Table 2.1, two models very well matched and the effects of the tissue structural change were consistent. In both models, the structural change from UN to BW increased CV and decreased $\dot{V}_{max}$ and the difference between UN and BW decreases as the gap conductance increases.

Table 2.1: CV/$\dot{V}_{max}$ during longitudinal propagation for 2D FEM and 2D FDM model (Hubbard, Ying et al. 2007). CV is in cm/sec and $\dot{V}_{max}$ is in V/sec

Structure	model	$g_j = 0.01\mu S$	$g_j = 0.1\mu S$	$g_j = 1\mu S$
UN	2D FEM	7.7/382	36.8/337	66.0/244
	2D FDM	7.0/377	35.9/322	66.5/253
BW	2D FEM	18.9/341	50.5/244	68.6/239
	2D FDM	18.2/343	49.6/258	67.7/241

2.3.2 Comparison to the three dimensional model with structured tissues

With UN and BW tissue structure, two dimensional FEM model was compared to three dimensional models to test the effects of depth discretization and gap junction distributions. As shown in Table 2.2, the behaviors of the models by the structural change were consistent and there was little difference between models. At the highest gap conductivity ($g_j = 1\mu S$), the largest CV difference occurred but the difference is less than 3%.

Table 2.2: CV/$\dot{V}_{max}$ during longitudinal propagation for two dimensional model and three dimensional model. CV is in cm/sec and $\dot{V}_{max}$ is in V/sec.

Structure	model	$g_j = 0.01\mu S$	$g_j = 0.1\mu S$	$g_j = 1\mu S$
UN	2D	8.8/382	40.4/330	73.2/243
	3DU	8.8/382	40.4/330	72.6/243
	3DC	8.8/383	40.0/331	71.4/245
	3DR	8.8/382	40.0/330	71.4/244
BW	2D	20.5/335	55.0/243	75.1/240
	3DU	20.5/335	54.3/242	75.8/239
	3DC	20.5/335	54.3/242	74.5/239
	3DR	20.5/335	54.3/242	74.5/240

2.3.3 AP propagation in a unstructured tissue

The effects of depth discretization and gap junction distribution were tested in RT tissue structure. In the two dimensional model, the gap junction conductance was set as 83.3 μS to achieve physiologically reasonable CV. This conductance was properly scaled in three dimensional models depending on the gap junction distributions. After stimulating the upper right corner cell in the tissue, the activation time was measured at the time when AP upstroke passes 0 mV and this was plotted in Figure 2.5. Although the models had different distributions of gap junctions in three dimensional space, little difference was found in the activation patterns between the models. The 3DR model did not keep the symmetry condition for the two dimensional model but it still showed little difference. To see the difference between models in more detail, the CV was measured along the marked lines in Figure 2.5 A and the result is summarized in Table 2.3. The Table 2.3 shows that, compared to two dimensional model, 3DU model's CV was exactly same but 3DC and 3DR model's CV was lower than that of two dimensional model. The difference among 2D, 3DC, and 3DR increased as the CV increased and the CV difference reached about 5% when CV in two dimensional model was the highest at 82 cm/sec. In addition to this, the waveforms sampled at marked locations in Figure 2.5 B were compared in Figure 2.6 but there is no visible difference between the methods.

Table 2.3: The path length in μm and CV in cm/sec along the path marked in Figure 2.5A.

Path number	1	2	3	4	5	6	7
Path length	380	104	201	84	134	36	307
2D	45.7	14.4	12.3	26.4	70.2	3.0	82
3DU	45.7	14.4	12.3	26.4	70.2	3.0	82
3DC	44.6	14.2	12.3	25.6	70.2	3.0	77.9
3DR	45.2	14.2	12.3	26.4	66.7	3.0	70.0

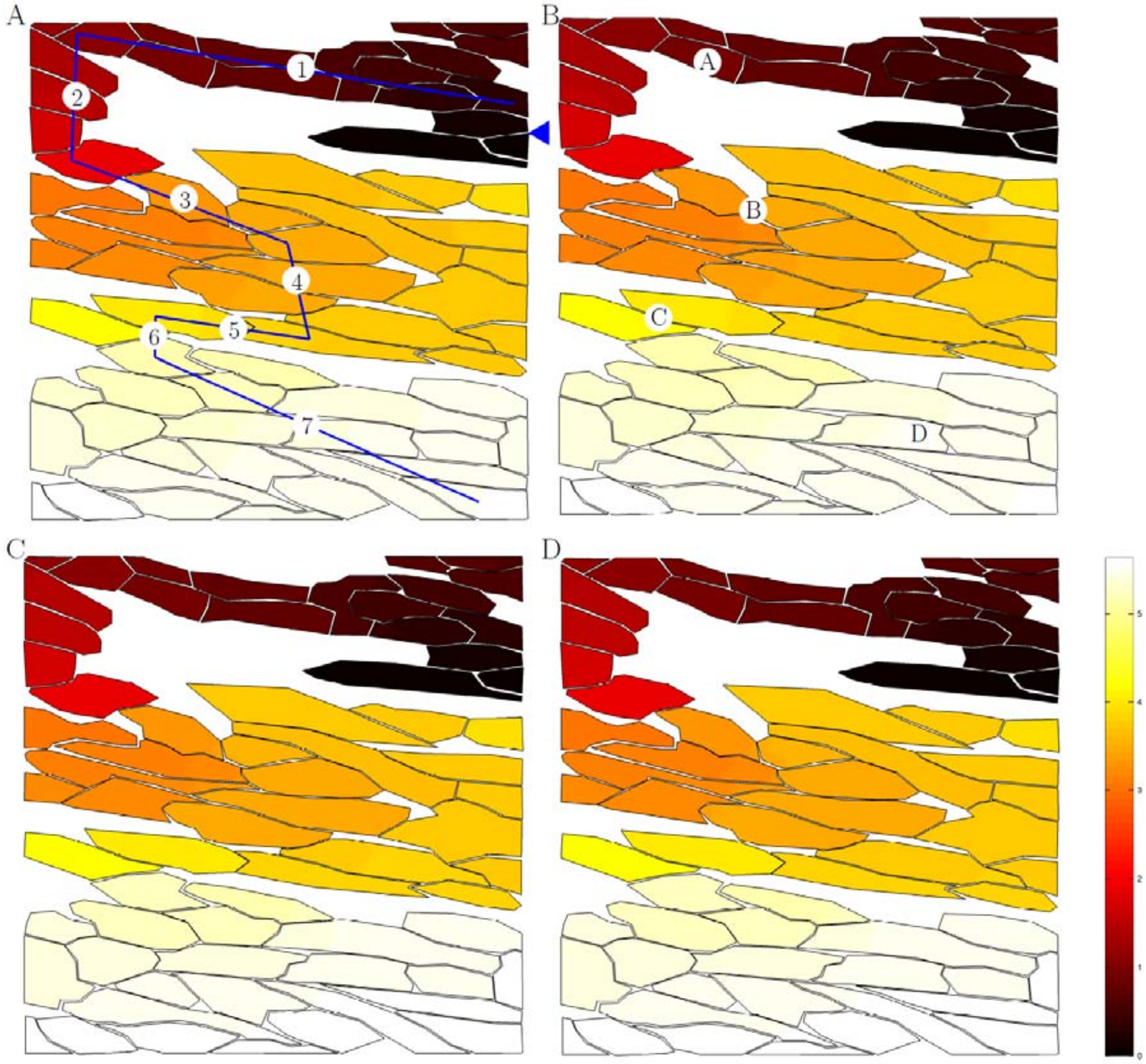

Figure 2.5: The tissue was stimulated by current injection at the node indicated by the arrow head on the upper right corner of the tissue. The blue lines crossing the tissue in two dimensional model indicates CV measurement reference. A. 2D, B. 3DU, C. 3DC, and D. 3DC

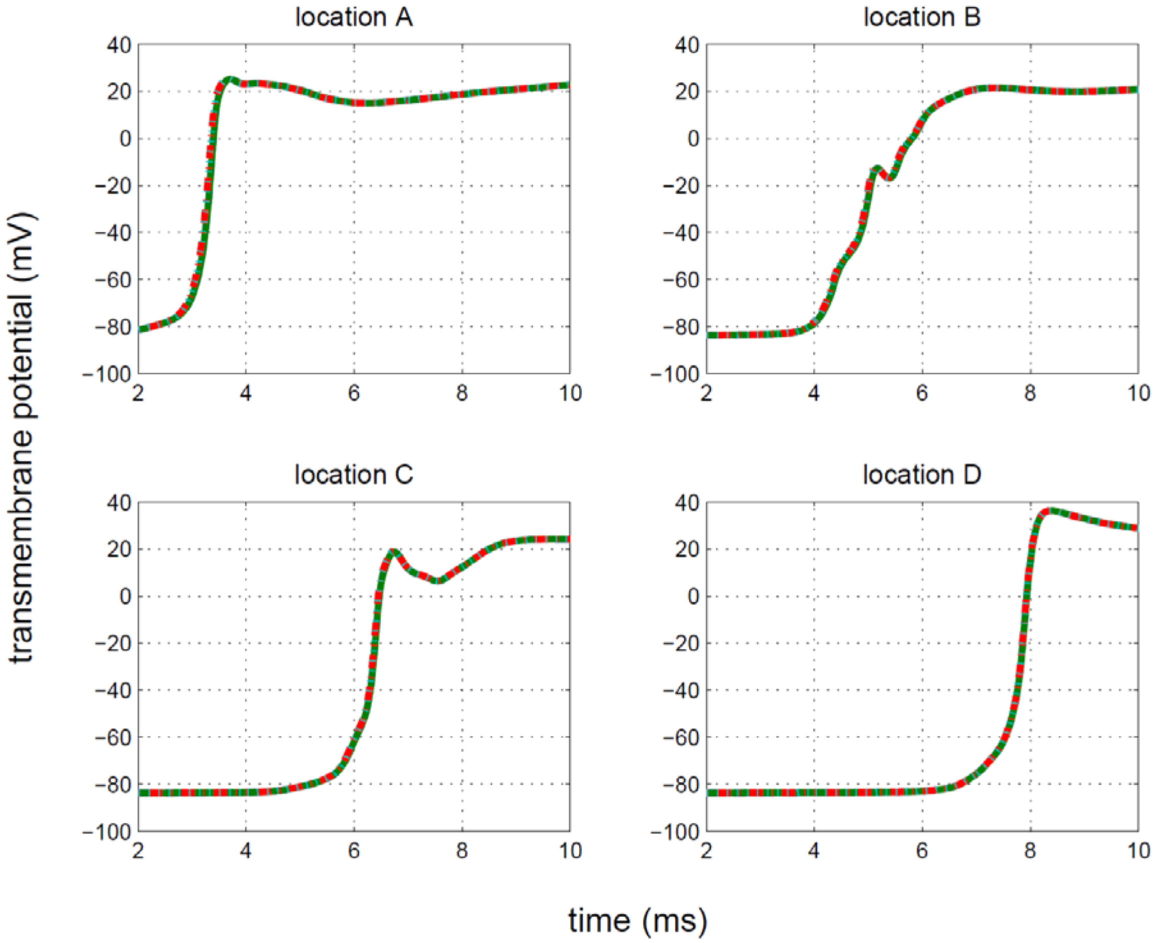

Figure 2.6: AP propagations at the marked locations in Figure 2.5 B. Solid line is for two dimensional model, dashed line is for 3DU model, dashed dot line is for 3DC model and dotted line is for 3DR model. They are overlapped and indistinguishable to each other.

2.4 Discussion

In this study, we developed a computationally efficient two dimensional model to simulate AP conduction in a monolayer tissue with arbitrary shaped cells. This method was derived from the three dimensional FEM by reducing the number of variables to improve the efficiency of the method under the symmetry condition of a monolayer tissue in the depth direction. This two dimensional model was compared with two dimensional FDM and there were no significant differences in CV and $\dot{V}_{max}$. Additionally this two dimensional model was tested by comparing CV and $\dot{V}_{max}$ from the three dimensional models because the accuracy of the two dimensional model can be degraded by two reasons. First, the two dimensional model was reduced from the three dimensional FEM model with single element in depth direction and the intracellular potential in depth direction was assumed almost constant. However, in the actual tissue, current can flow through membrane and a nonzero potential gradient can exist normal to membrane. This can result in varying intracellular potential in depth direction. Second, the distribution of the gap junctions can increase the nonlinearity of the intracellular potential. The two dimensional model had the gap junctions located on one dimensional boundary edges but the three dimensional models had the gap junctions on two dimensional boundary faces which enables the three dimensional models to have many possible gap junction distributions on two dimensional boundary faces satisfying the symmetry condition and having identical projection on one dimensional boundary edges. Among the possible gap junction distributions, some of them could increase the nonlinearity of the intracellular potential. Thus the effects of these two were numerically tested by comparing the two dimensional model and the three dimensional models with fine depth discretization and three kinds of distributions of gap junctions. For the comparison, we built 3 types of tissue structures, UN, BW, and RT with three kinds of three dimensional models, 3DU, 3DC, and 3DR. The AP propagation results showed that, if the tissue structure was same, there were less than 5% difference in CV and $\dot{V}_{max}$ when the cells were well coupled with high gap junction conductivity. The Table 2.2 and 2.3 showed that the gap junction differences affect the behavior of the model when the cells are well coupled and CV is high because the nonlinear intracellular potential can slow down only while AP propagates through intracellular space. When the cells are less coupled and most of the delay occurs at gap junctions, the three dimensional gap junction distributions have little effect.

Bursac et al. cultured neonatal cardiac tissue on fibronectin by using microabrasion and micropatterning so that anisotropy ratio and fiber direction in a tissue can be controlled (Bursac, Parker et al. 2002). While this technique provides a good experimental tool to study the effect of heterogeneity of the tissue on AP propagation, the model can provide additional insight. The modeling approach can duplicate structural heterogeneity of the cultured tissue from the microscopic images. If the electrical properties of the tissue are assigned properly, the model can reproduce the heterogeneous features of AP propagation in the tissue at the scale of a single cell.

This model could be extended to simulate a multilayer tissue or to include extracellular stimulations. In multilayer tissue model, the depth directional symmetry disappears and each cell needs to be described as a complete three dimensional structure. Extracellular space stimulations are more complicated because the spaces between cells distort the electric field and the effects of the distorted electric field need to be assessed before any approximations. Our model is flexible in describing the tissue morphology but it is computationally more expensive than the other methods using the structured grids. This is in part because our model needs more nodes to describe the irregular cell boundaries which results in larger linear system and in part because solving the linear system produced from the unstructured grid tends to be less efficient compared to that from the structured grid. In order to simulate large tissue, the model can be improved by using efficient preconditioners or reducing the number of nodes in the model. One of the most efficient preconditioner in FEM modeling is ones based on multigrid but using multigrid in our model can be challenging because of use of unstructured grids (Briggs, Henson et al. 2000) and the fact that the system is not symmetric positive definite. However the cells in the tissue were discretized separately and this discretization produces the linear system as a blocked matrix. For this system, preconditioners based on block ILU or domain decomposition can be efficient. One way of reducing the number of nodes in the model can be building a hybrid model using both structured grid for well coupled parts of the tissue and unstructured grid for less coupled parts of the tissue. The well coupled tissue behaves as a continuous medium, which can be modeled with structured grids. These grids tend to require fewer nodes so that the hybrid model can use fewer nodes for the well coupled part of the tissue. Our two dimensional FEM model can simulate a monolayer tissue with arbitrary shape and its behavior is consistent with that of three dimensional model. The model can be built by obtaining cell boundaries from the tissue image and assigning connections for gap junctions. Because of its flexibility in modeling the tissue morphology, this model can be useful tool for studying interactions between AP propagation and the tissue structure.

3. A Computer Model of Engineered Cardiac Monolayers

This chapter was adapted from a paper that recently was accepted for publication in the Biophysical Journal (Kim, Bursac et al. 2010).

3.1 Introduction

The anisotropy in electrical properties arising from the distribution and coupling of cardiac cells in tissue has been shown to have a significant impact on impulse initiation and propagation (Leon and Roberge 1991; Fast and Kleber 1994; Spach and Heidlage 1995; Spach, Heidlage et al. 2000; Bursac, Parker et al. 2002). Changes in anisotropy often arise in certain cardiac pathologies such as ischemia, infarction, and heart failure (Carmeliet 1999; Cleutjens, Blankesteijn et al. 1999; Li, Fareh et al. 1999). This change is usually related to altered gap junction distribution and/or expression, and the formation of collagenous septa between the cardiac fibers and groups of cells that result in discontinuous transverse propagation (Spach and Dolber 1986). While it is known that the type, amount, and distribution of gap junctions in the cell membrane, the cell size and geometry, and the interconnectivity of cells determine the magnitude of anisotropy of tissue, studying the separate effects of each of these factors experimentally has been challenging (Spach, Heidlage et al. 2000; Bursac, Parker et al. 2002).

Recent advances in tissue engineering and micropatterning techniques have made it possible to create monolayers in which the degree of anisotropy can be reproducibly controlled. Bursac et al. presented an *in vitro* model system that enables systematic manipulation of the degree, orientation, and nonuniformity (continuity) of anisotropy in centimeter-sized monolayer cultures of neonatal rat cardiac myocytes (Bursac, Parker et al. 2002). Using micropatterning, they cultured series of cardiac monolayer tissues whose microscale continuity changes from discontinuous to continuous and the cell orientations change from oriented (anisotropic) to disoriented (isotropic). While these experimental monolayers allow for sophisticated electrophysiological, pharmacological, and genetic studies of simple impulse propagation and reentry dynamics *in vitro*, they are currently limited to neonatal cells with electrophysiological properties that differ from humans. In addition, some features of the tissue, like the magnitude and distribution of gap junctions, are not easy to control locally.

Another approach for studying the impact of tissue cellular structure on conduction is to make use of computer models (Leon and Roberge 1991; Spach and Heidlage 1995; Shaw and Rudy 1997; Spach, Heidlage et al. 2000; Hubbard, Ying et al. 2007). Many models of cardiac tissue assume continuous properties, where the electrical properties are usually assigned to match the observed, macroscopic conduction velocities in the tissue and account for macroscopic variations in fiber orientation (Henriquez 1993; Sampson and Henriquez 2002; Qu 2006). Another approach to model cardiac tissue is to explicitly represent the coupling between cells or fibers. Leon et al. presented a discrete cable model connected with regular array of identical resistors such that the discontinuity of the tissue only appeared in transverse direction (Leon and Roberge 1991). This approach has been extended to consider more complex anisotropy (Vigmond and Leon 1999). Spach et al. modeled a tissue as individual cells whose cell boundaries were duplicated from isolated cardiac cells and the gap junctions were arranged similar to the experimental observations (Spach and Heidlage 1995). In the coupled cable approach, the cell shapes have been idealized to be cylindrical, limiting the random variation in cell size and coupling observed in native tissue. In the models used by Spach et al., the shape of the cell is constrained to map to a rectangular Cartesian grid, limiting the ability to study the effects of random cell orientations.

While simulations of Spach et al.'s discrete models have revealed that changes in cell sizes and the distribution and the coupling strength of gap junction can influence the conduction velocity, the relationship of these changes in tissue structure to the macroscopic conductivities has not been fully elucidated (Spach, Heidlage et al. 2004). One of the challenges is that it is not always clear how to obtain the effective conductivities in multidimensional discrete tissue with random structure that involves variations in cell shape, orientations and coupling. In this paper, we present a novel approach to modeling discrete cardiac tissue in which the factors governing cell shape, cell-to-cell coupling and the degree of cleft space are not constant but rather are spatially random with assigned distributions. Using this approach, it is possible to construct a number of random cellular networks with different tissue features yet possess statistically similar macroscopic behavior. By creating several realizations of the same tissue, it is possible to perform simulations in a manner analogous to performing experiments on engineered tissue with natural variations from monolayer to monolayer. We also present a global and a local approach to obtain the macroscopic conductivities from these random networks. The simulations reveal that under normal ranges, global changes in cell shape and connectivity are manifested as changes in the effective macroscopic intracellular tissue conductivities that result in differences in both the macroscopic conduction velocities and the conduction velocity anisotropy ratios. The results show that over a normal range of parameters a continuous model with appropriately assigned conductivities can explain measured conduction velocities in discrete cardiac tissue with complex microstructure. The variance of the global estimates, however, increases with increasing degree of discreteness (i.e. cleft space). The results also reveal that in the presence of abrupt changes in cell orientation, local estimates of the conductivities predict smoother changes in conductivities that may not adequately predict the discrete nature of propagation at the transition sites.

3.2 Methods

3.2.1 Generation of Discrete Tissue Pattern

The simulated tissue was generated by 1) defining template cells, 2) modifying the cell shapes and 3) adding clefts (Figure 3.1 A-C). The tissue domain was populated with non-overlapping “elliptical” template cells with assigned orientations and locations. To accomplish this, a template cell of 120 μm in length and 24 μm in width was first generated at top right of the domain. This cell was moved toward the bottom left until it can no longer move due to presence of other cells or the boundaries of the domain. Upon the placement, each template cell was rotated with an angle drawn randomly from a normal distribution, thus controlling the alignment of the cells in the tissue. This process was repeated until the domain was filled with the template cells. Once the template cells filled the domain, cell shapes were modified to fill the gap between cells. A cell was selected in random order and the boundary of this cell was expanded, by moving randomly selected boundary points away from the cell center by a small amount without overlapping with neighboring cells. This expansion was repeated several times for all the cells in the tissue while reducing the amount of expansion gradually. Finally, clefts were incorporated in the tissue by shrinking the width of randomly selected cells. To accomplish this step, each cell was assigned a random number drawn from a uniform distribution between 0 and 1. Cells whose assigned random numbers were smaller than cleft probability were selected to be reduced in size. The selected cell was reduced by moving each boundary point toward the cell's longitudinal line, which passes through the cell center in the length direction. The resulting tissue contained random shaped cells whose orientations followed the orientations of the templates. The cell orientation was controlled by the standard deviation of the normal distribution while the amount of cleft space was controlled by cleft probability.

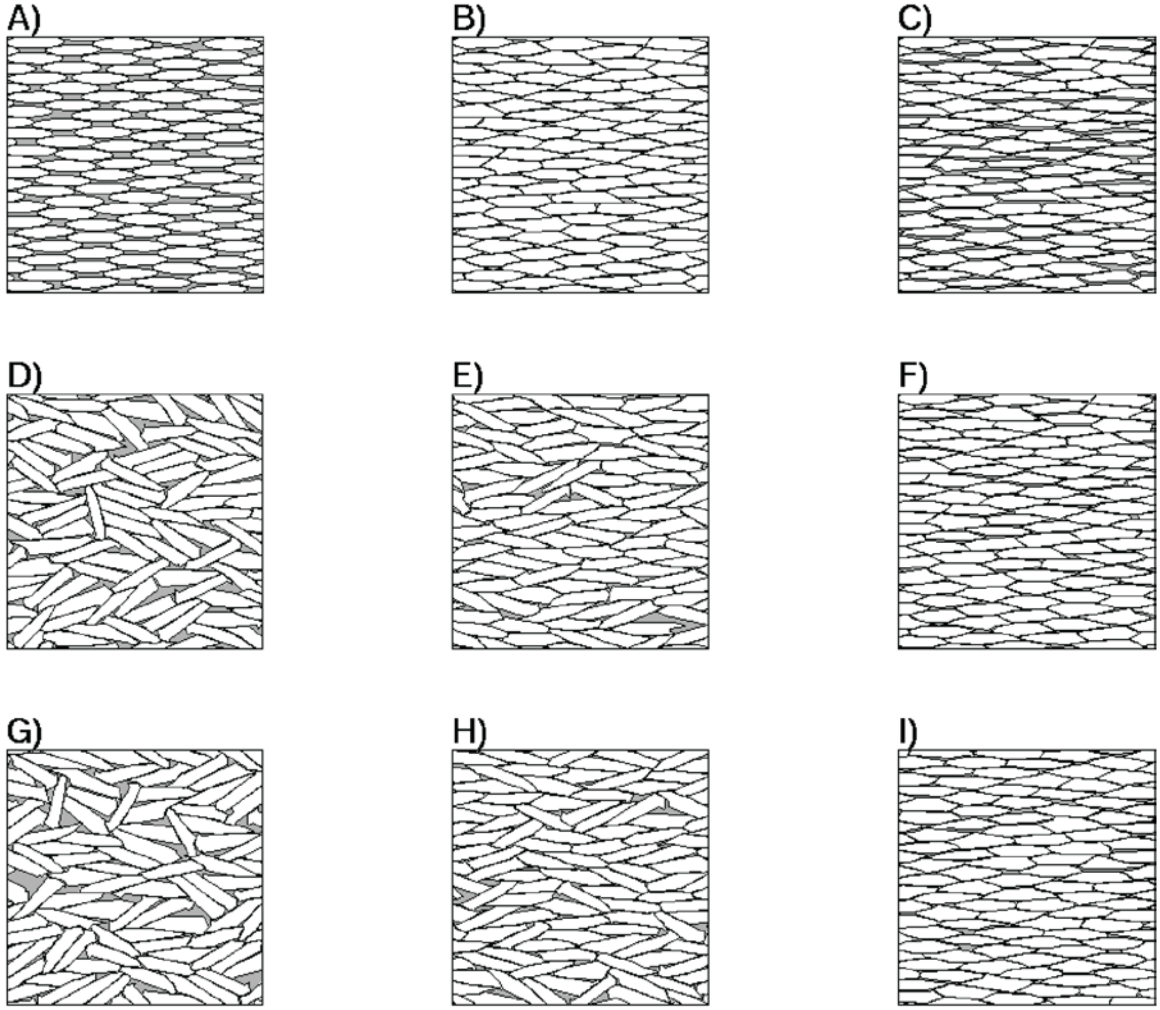

Figure 3.1: A)-C) show the procedure generating the tissue pattern. A) placing template cells, B) changing shapes of cells (cell angle standard deviation = 0.02), C) adding clefts (cleft = 0.5) D)-I) show tissue patterns with various tissue generation parameters. Different cell distributions appear from tissues sharing the same generation parameters. D,G) (cell angle standard deviation = 0.5, cleft = 0) E,H) (0.25, 0) F,I) (0.02, 0.25). All panels show 500 μm by 500 μm area.

3.2.2 Effective tissue conductivity measure

Two methods (global and local) were used to estimate the effective conductivity of the intracellular space. In the global method, the membrane elements were removed, leaving only the passive intracellular network that contained both the intracellular space of the cells and the coupling conductance between cells. This method is also referred to as the equivalent circuit method. For regularly arranged cells, the effective conductivity can be obtained analytically. For example, if the tissue is composed of rectangular cells that are stacked on top of each other with uniform width W and length L and if gap couplings are uniform along the cell borders with a coupling strength per unit contact area given by g, then the effective tissue conductivity can be written in the following form:

$$\sigma_L = \frac{Lg\sigma}{Lg + \sigma} \tag{3.1}$$

$$\sigma_T = \frac{Wg\sigma}{Wg + \sigma} \tag{3.2}$$

where σ, σ_L, and σ_T are intracellular conductivity, longitudinal tissue conductivity, and transverse tissue conductivity, respectively. For the tissues with irregularly shaped cells and connectivity, a numerical approach can be used to obtain the effective properties. To accomplish this, cells at one edge of the tissue were grounded and current was injected into the cells at the other edge through discrete current sources. The potential was measured through the tissue and the total injected current was measured by summing up the all discrete sources. This measured potential was then used to estimate the electrical field strength E defined as negative gradient of potential, by performing a linear fit of the potential and the distance from the current source.

$$V = -Ex + b \tag{3.3}$$

The effective conductivity σ was estimated by the ratio between current flux and electrical field strength.

$$\sigma = J/E \tag{3.4}$$

where current flux J was obtained from the sum of the injected current divided by the cross sectional area of the tissue. This method was independently applied in the longitudinal and transverse directions to obtain the conductivities in each direction.

A local method for estimating the effective intracellular conductivity was also developed. In principle, this method can be experimentally implemented. This method consisted of two steps: 1) estimating passive membrane resistance R_m from the transmembrane potential of an isolated cell subject to a subthreshold stimulus and 2) estimating effective tissue conductivity from the steady state membrane potential. In the first step, the passive membrane resistance R_m was estimated from the measured subthreshold time response from a single, isolated cell from the model using simple RC circuit analysis.

$$V = V_0 + (V_S - V_0)\exp\left(-\frac{t}{R_m C_m}\right) \tag{3.5}$$

where V_0 and V_S are the initial and steady state potentials, respectively. Under the assumption that the membrane capacitance $C_m = 1\mu F/cm^2$, the membrane resistance R_m

was estimated from this equation and the measured time response of the membrane potential. In the second step of this method, the subthreshold point stimulus was applied at the center of the discrete tissue. If the stimulus pulse is long enough, the membrane capacitance is assumed to be fully charged at steady state. The steady state membrane potential of the discrete tissue was compared with that of the continuous tissue with the membrane replaced by the membrane resistance R_m and whose conductivity was systemically changed to minimize the error between steady state membrane potential obtained from the discrete tissue and that obtained from the continuous tissue. The longitudinal and transverse conductivities of the continuous tissue model minimizing this error were considered to be the corresponding effective conductivities of the discrete tissue model. The Levenberg-Marquardt algorithm was used for the numerical estimation (Lourakis 2004). This method is also referred to as the subthreshold response method.

3.2.3 Numerical and Computational Methods

Because of the computational efficiency, the membrane kinetics were described with the model proposed by Bueno-Orovio, Cherry and Fenton (Bueno-Orovio-Cherry-Fenton-Karma model) (Bueno-Orovio, Cherry et al. 2008), based on the model initially published by Fenton and Karma (Fenton and Karma 1998) with parameters in Table 3.1 was fit to match the Wang-Sobie (WS) model (Wang and Sobie 2008) of a neonatal mouse cell, which has a shape and duration that resembles neonatal rat cells. These parameters were found by fitting the action potential's upstroke and derivative while it propagated as a planar front in the two-dimensional monolayer (FK $\dot{V}_{max} = 62.0\ V/sec$, $APD_{90} = 83.0\ msec$; WS $\dot{V}_{max} = 50.0\ V/sec$, $APD_{90} = 71.0\ msec$).

Table 3.1: Bueno-Orovio-Cherry-Fenton-Karma model parameters

u_0	0	u_u	1.55	θ_v	0.382	θ_w	0.286	θ_v^-	0.000736	θ_0	0.00063
τ_{v1}^-	14.929	τ_{v2}^-	1015.43	τ_v^+	2.695	τ_{w1}^-	53.45	τ_{w2}^-	8.059	k_w^-	74.827
u_w^-	0.01	τ_w^+	239.077	τ_{fi}	0.186	τ_{o1}	540.026	τ_{o2}	10	τ_{so1}	35.436
τ_{so2}	2.145	k_{so}	1	u_{so}	0.991	τ_{s1}	4.681	τ_{s2}	3.013	k_s	1.656
u_s	0.997	τ_{si}	11.679	$\tau_{w\infty}$	0.493	w_∞^*	0.857				

The cell thickness was assumed to be 16 μm and the intracellular conductivity was 6.67 mS/cm. Gap junctions were distributed uniformly around the cell border with nominal coupling strength of 0.1667 mS/cm. If the boundaries of two neighboring cells were closer than 1μm in the cell boundary image, they were connected via a gap junction. Except for the cases where the cell alignments and cell length/width ratio were changed (Figure 3.5), five types of tissues were considered by increasing the number of clefts with constant cell alignments. The cells in these tissues were generated with an elliptical template cell of 120 μm in length and 24 μm in width. The parameters for the five tissue types are summarized in Table 3.2. For each type, eight realizations of the tissues were produced, to obtain average properties. Example tissues are shown in Figure 3.1 and Figure 3.3. The average length, width and area of cells are summarized in Table 3.2.

Table 3.2: Tissue generation parameters and cell length, width, area and density of resultant tissues. STD = standard deviation, values in parenthesis are standard deviations

	TC0	TC1	TC2	TC3	TC4
Cell angle STD	0.02	0.02	0.02	0.02	0.02
Cleft probability	0	0.1	0.2	0.3	0.4
Length (μm)	137.5 (10.5)	137.5 (10.5)	137.5 (10.5)	137.5 (10.5)	137.5 (10.5)
Width (μm)	28.0 (3.4)	27.8 (3.5)	27.4 (3.6)	26.8 (3.8)	26.1 (4.1)
Area (μm^2)	2417 (233)	2391 (243)	2349 (264)	2292 (292)	2220 (323)
Density (cm^{-2})	39449 (29)	39450 (28)	39450 (29)	39448 (30)	39449 (32)

All domains were approximately $7.5mm$ long and $5mm$ wide. A $1msec$ long unipolar stimulus, which was $2-3$ times greater than threshold, was applied to initiate propagation. The generated tissue patterns were discretized using the software package Triangle, a Delaunay triangular mesh generator (Shewchuk 2002). Domains were generated such that the triangle areas did not exceed 50 μm^2 and no angles in the triangles were smaller than 28.5 degrees, except for those triangles at the boundaries (Figure 3.2). A typical domain had approximately 860,000 nodes. The monodomain model from the chapter 2 was solved using the FEM and Crank-Nicolson method with a time step of $25\mu sec$ (Keener and Bogar 1998). The resultant linear system was solved by the Unsymmetric MultiFrontal method in UMFPACK (Davis and Duff 1997).

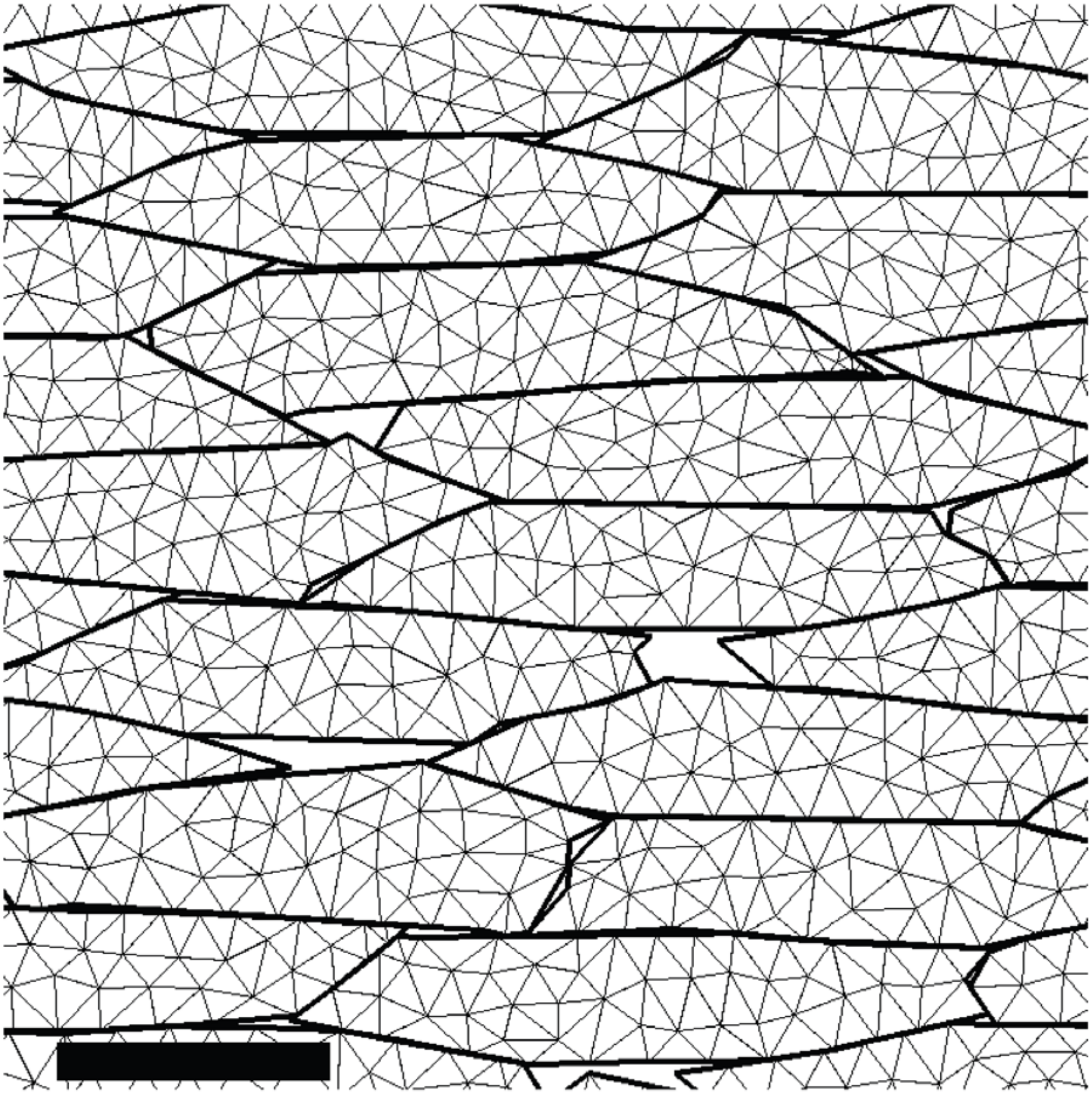

Figure 3.2: Cell discretization for FEM was generated by Triangle (Shewchuk 2002). The thick line indicates cell boundaries and the scale bar on lower left corner is 50 μm long.

3.3 Results

3.3.1 Propagation through irregular shaped cells

Using the tissue generation method described above, domains with different degree of cell orientations and amount of cleft space were created. Since a tissue was generated from randomly populated elliptical template cells, the simulated tissues contain some holes even when no clefts were intentionally added (Figure 3.1 D and G). The placement and shape of each template were controlled by random numbers, enabling the generation of unique cell boundaries even when the tissues were generated from the same parameters (Figure 3.1 D - I).

Figure 3.3 shows cell boundaries of three example tissues. Tissue TC0 had no cleft space, mimicking ideal confluent monolayers. In tissues TC2 and TC4, the cleft probabilities were 0.2 and 0.4, respectively. The space between cells increased from TC0 to TC2 and TC4, resulting in smaller contact area between cells. Figure 3.3 B shows a histogram of cell-cell contact length. Adding clefts slightly reduced the average of cell-cell contact length and changed the statistical distributions. There is little difference in overall cell size except the widths decrease from 28.0 μm at TC0 to 26.1 μm at TC4. The tissue generation parameters, average cell length, width, area and density in each tissue type including TC1 and TC3 are shown in Table 3.2.

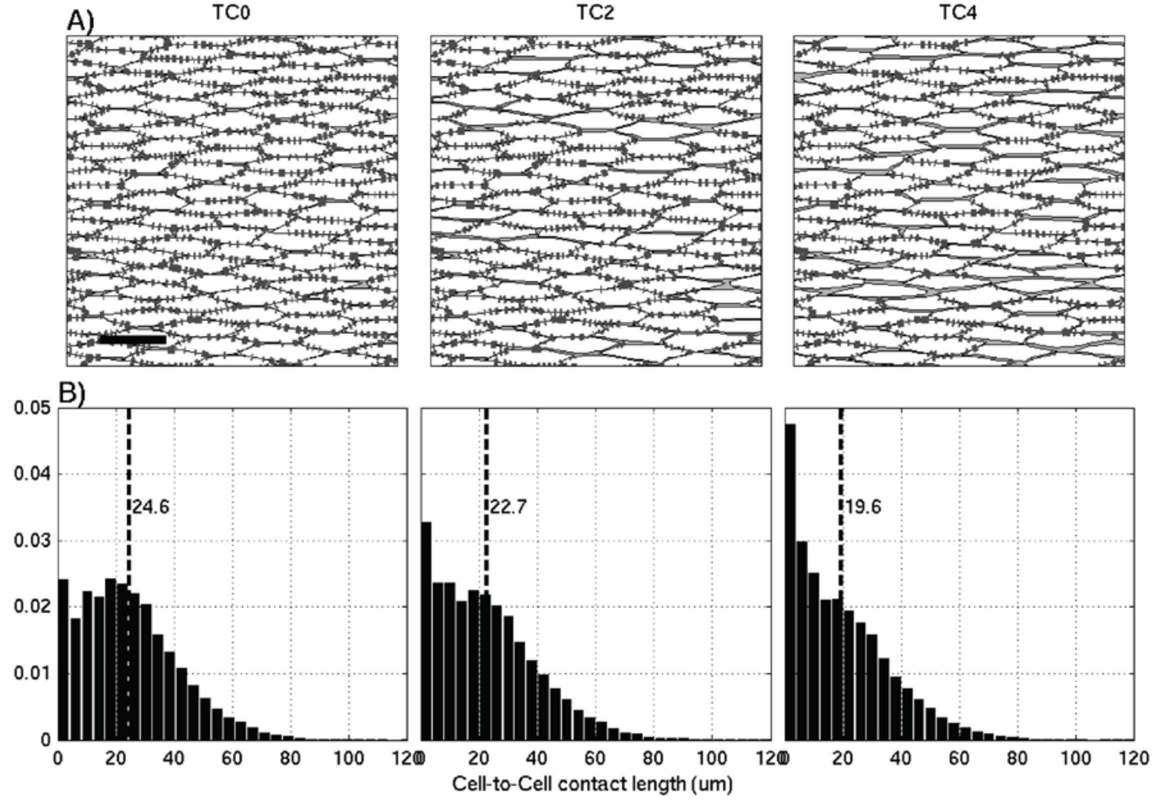

Figure 3.3: A) Cell boundaries in TC0, TC2 and TC4 tissues. Dark gray indicates gap couplings and light gray indicates extracellular space. The scale bar is 100 μm long. B) Cell-cell contact length histogram. Dashed line indicates average contact length. Because of the model assumption, gap coupling strength is proportional to the cell-cell contact length.

Figure 3.4 shows the activation patterns generated in the three example tissues arising from a point stimulus at the macroscopic and microscopic levels. At the macroscopic scale, the wavefronts are roughly elliptical in all models. In contrast to a continuous model with uniform and smooth wavefronts, however, the wave in the simulated discrete tissues propagates less regularly at the microscale, due to the cell boundaries and distributions of gap junctions. As more cleft space is added, the microscopic fronts become more irregular. The macroscopic conduction velocities in the fast longitudinal direction (LCV) and in the slow transverse direction (TCV) slowed with increasing cleft density. In addition, the conduction velocity anisotropy ratio (AR=LCV/TCV) increased as a result of increased microscopic heterogeneity. These effects of the microscopic changes on the CV changes are summarized in Table 3.3.

Table 3.3: CV and AR measured from a front arising from a planar stimulus and point stimulus. Values in parenthesis are standard deviations.

	TC0	TC1	TC2	TC3	TC4
			Front from a planar stimulus		
LCV (cm/sec)	38.4 (0.09)	36.6 (0.16)	33.2 (0.24)	28.9 (0.32)	24.3 (0.75)
TCV (cm/sec)	10.3 (0.05)	8.9 (0.06)	7.4 (0.07)	5.9 (0.1)	4.4 (0.18)
AR	3.74 (0.02)	4.10 (0.03)	4.49 (0.04)	4.89 (0.08)	5.46 (0.18)
			Front from a point stimulus		
LCV (cm/sec)	34.7 (0.44)	33.4 (0.99)	30.5 (0.91)	26.1 (1.84)	20.9 (1.75)
TCV (cm/sec)	9.3 (0.2)	8.2 (0.19)	6.6 (0.26)	5.4 (0.45)	3.8 (0.56)
AR	3.74 (0.11)	4.08 (0.2)	4.6 (0.24)	4.84 (0.66)	5.55 (0.85)

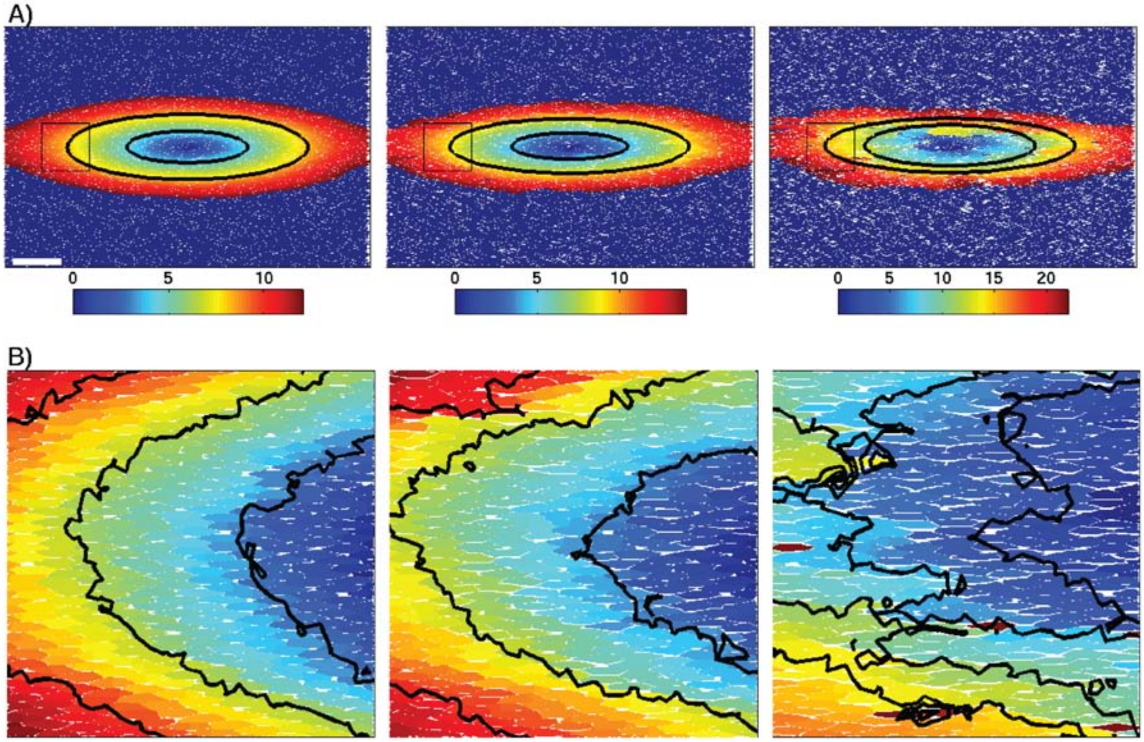

Figure 3.4: A) Activation time colormap of TC0, TC2 and TC4 tissues at 12, 14, and 22 *msec* after the stimulus onset. The scale bar at the bottom left is 1 *mm* long. B) 1 *mm* by 1 *mm* area marked at the upper panel shows detailed isochrones. Interval between isochrones is 1.7 *msec* in TC0 and TC2, and 2.0 *msec* in TC4.

3.3.2 Cell geometry and AP conduction

The increase in AR-CV with increasing cleft space is consistent with the experimental studies of Bursac et al. (Bursac, Parker et al. 2002). To further investigate the effects of the microscopic properties on conduction, simulations were performed in which the cell orientations and distribution of clefts were varied as a function of cell length/width ratio (CLWR). Figure 3.5 shows the LCV and TCV for various randomly generated tissues as a function of the AR. The simulations were designed to explain the results shown in Figure 8 in Bursac et al. (Bursac, Parker et al. 2002). In each panel, CLWR was changed from 3 to 6 while maintaining an average cell area. Initially, only the cell orientations in the models were varied by changing the cell angle standard deviation from 0.5 (isotropic, disoriented) to 0.02 (anisotropic, oriented) with zero cleft probability, to mimic confluent tissue. The isotropic, non-aligned tissues are shown to the left of the vertical dashed lines. For the anisotropic tissue with nearly aligned cells (cell angle standard deviation of 0.02), the amount of cleft space was increased by increasing the cleft probability from 0 to 0.4. These tissues are shown to the right of the vertical line. Increasing the alignment of cells in the confluent tissue tended to increase LCV and decrease TCV and thus increase AR. Increasing the cleft space, however, acted to decrease both LCV and TCV. The magnitude of the AR-CV transition point corresponding to the inclusion of clefts increased with increasing CLWR. In addition, the maximum and minimum LCV increased and the maximum and minimum TCV decreased with increasing CLWR. Table 3.4 summarizes the effects of cell geometry on AR and CV.

Table 3.4: Summary of AR-CV in Figure 3.5

Length/width ratio	3	4	5	6
Max LCV	26.6	31.4	35.9	39.6
Min LCV	15.2	16.0	17.0	17.4
Max TCV	11.8	11.3	11.1	10.9
Min TCV	4.6	3.1	4.0	2.1
AR at max LCV	2.4	3.2	3.9	5.0

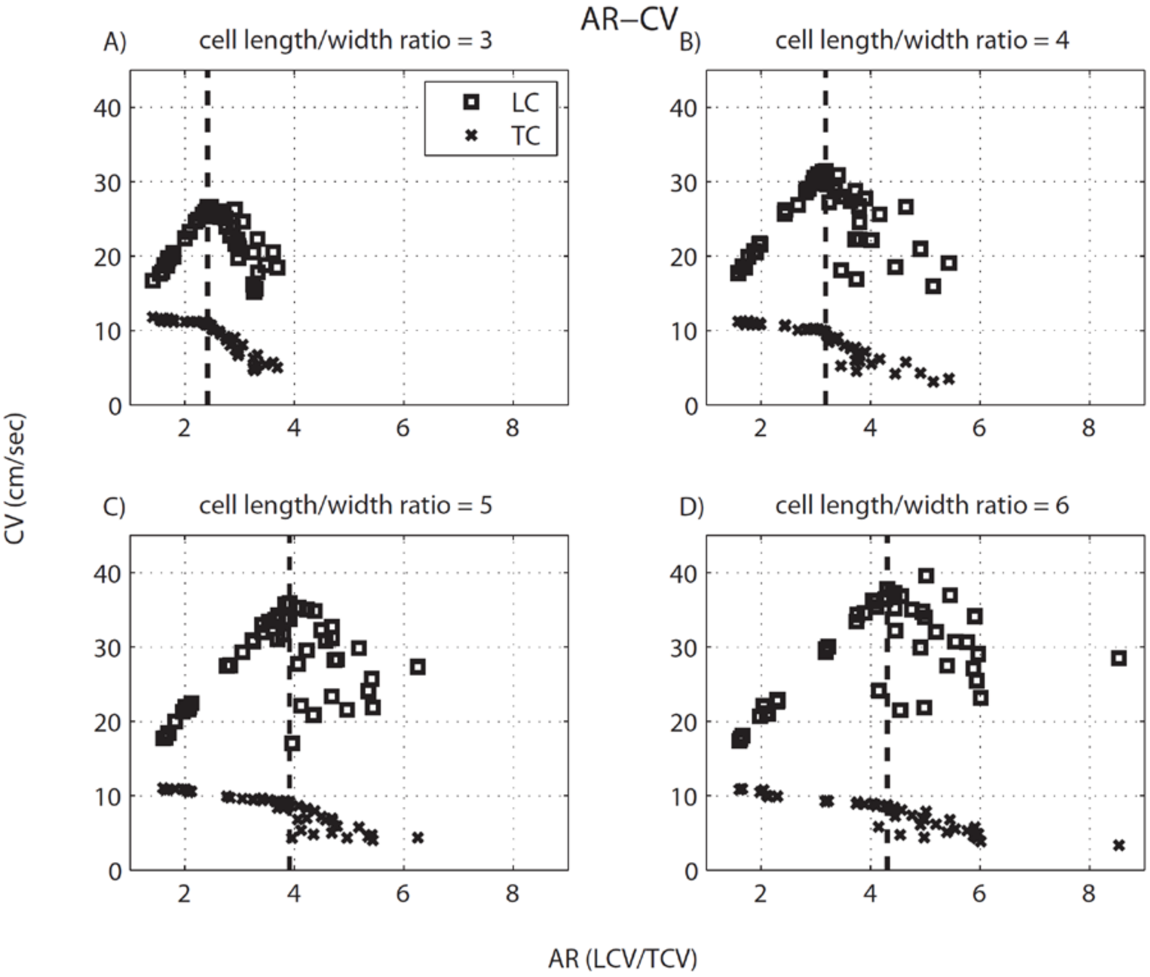

Figure 3.5: AR-CV plot with different cell length/width ratios, cell orientations and amount of clefts. The dashed line divides effects of cell orientations and clefts. The left of the dashed line shows changes in AR-CV due to cell orientations. The right shows changes in AR-CV due to clefts.

3.3.3 Gap coupling strength and AP conduction

There have been several experimental studies to study the effects of modulation of gap junction conductance through the application of certain pharmacological agents (Hennan, Swillo et al. 2006; Lin, Zemlin et al. 2008). One particular novel anti-arrhythmic approach has been proposed recently, in which the peptide rotigaptide is used to enhance gap junction conductance in infarcted regions to facilitate conduction (Hennan, Swillo et al. 2006). Unfortunately, precise experimental control of the conductance change is challenging. In the simulation studies, however, it is possible to modify the gap conductance uniformly or non-uniformly. Figure 3.6 shows the changes in AR, LCV and TCV after gap coupling was uniformly increased or decreased from its nominal value in five discrete tissues. LCV and TCV both increased monotonically with increasing gap coupling strength. The AR, however, was not statistically different for any of the gap strengths.

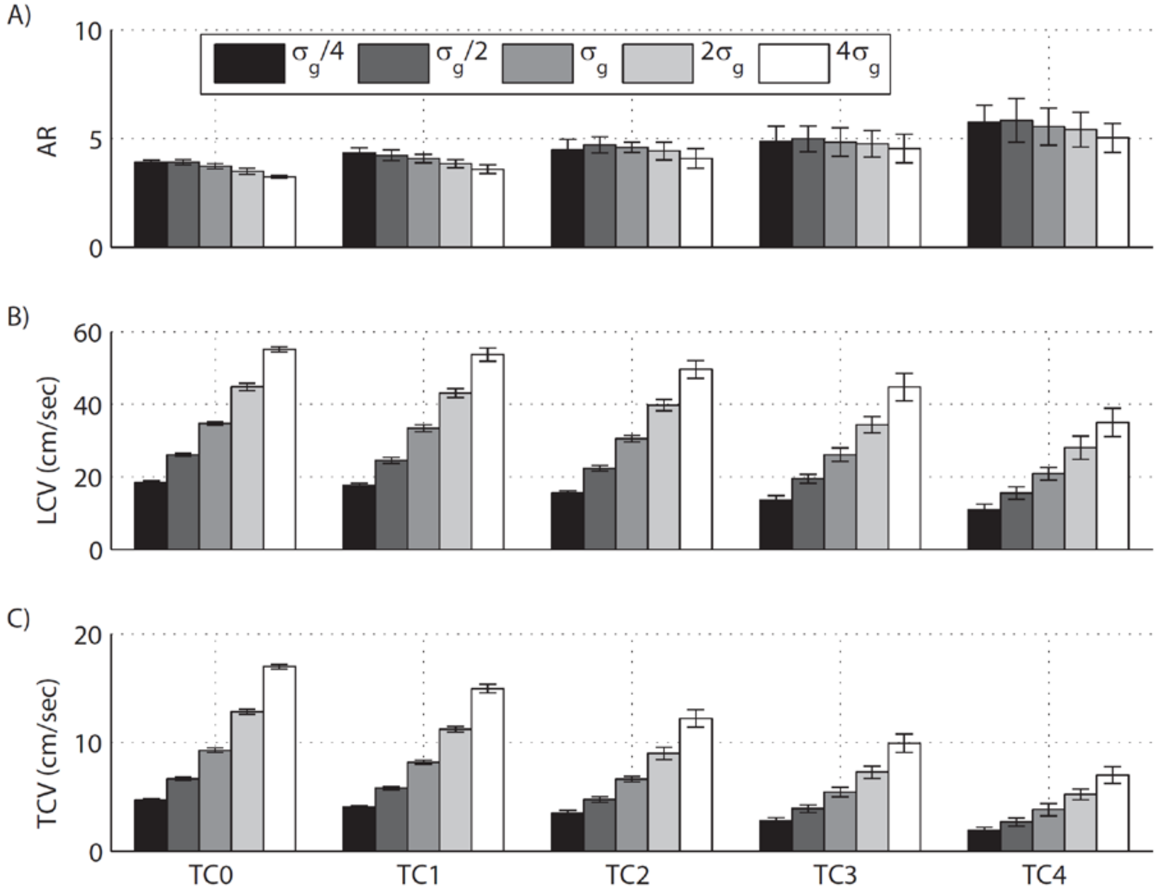

Figure 3.6: Effects of gap coupling strength on CV and AR. $\sigma_g = 0.1667\ mS/cm$. Both LCV and TCV increased monotonically by increasing gap coupling strength. AR did not show statistically significant change by gap coupling strength change.

The gap conductance can also be changed nonuniformly. A simulation was performed comparing the conduction velocities in tissues with varying degree of cleft space in which the gap coupling was uniformly increased by 200% for all gap junctions and nonuniformly increased in which the conductance of 50% of the gap junctions were increased 400% and the conductance of the other 50% of the gap junctions remained unchanged, such that the averaged gap coupling increase was 200%. A point stimulus was applied at the center of tissue and LCV, TCV and AR were measured. As shown in Figure 3.7, LCV and TCV were both faster for both the uniform and nonuniform gap coupling increase. The increase in the CV in the case where the gap junction coupling was uniformly increased, however, was greater than the case where the gap junction coupling was non-uniformly increased. The uniform case resulted in an average of a 50.7% and 62.4% speed-up in LCV and TCV, respectively, while nonuniform case resulted in an average of a 43.3% and 52.2% speed-up in LCV and TCV. This difference was statistically significant ($p < 0.05$). Although the TCV increase was larger than LCV increase, the AR decrease was statistically significant for uniform cases and for TC0 and TC1 in nonuniform cases ($p < 0.05$).

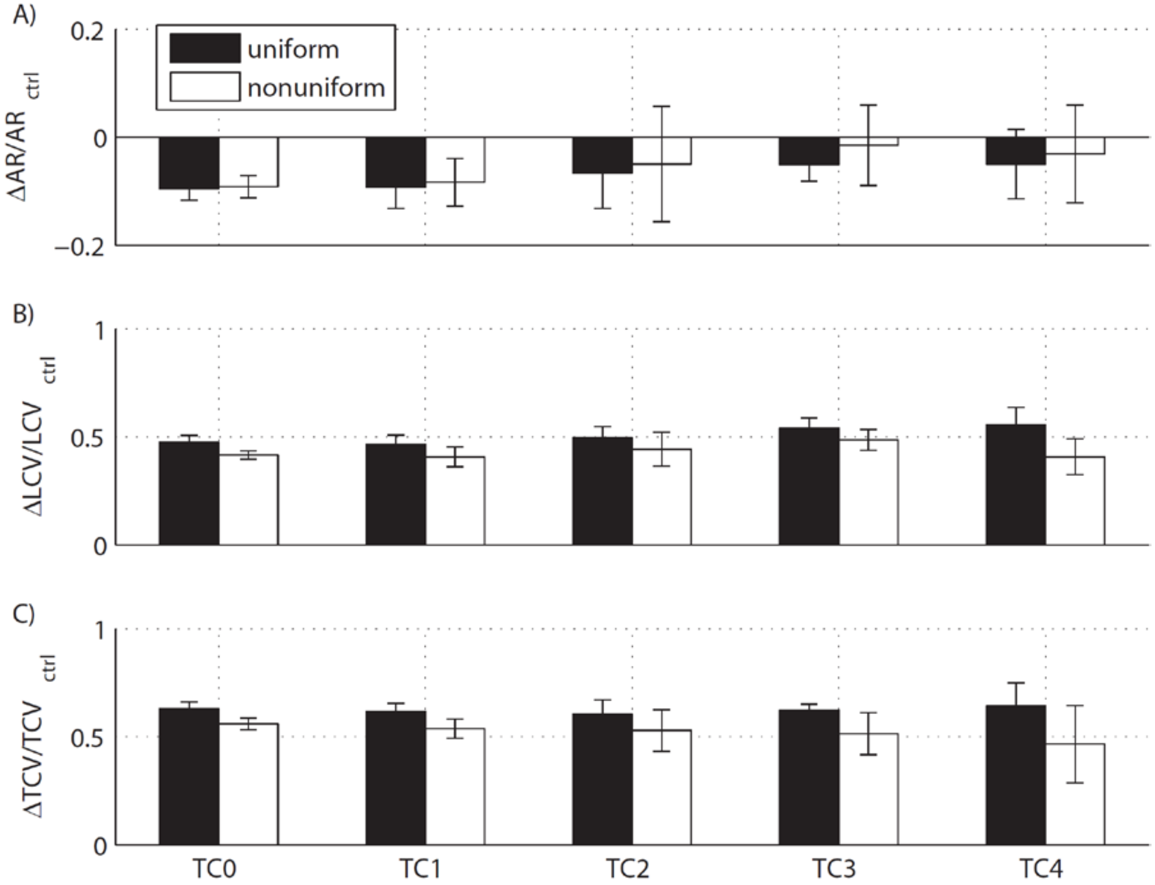

Figure 3.7: Changes in AR and CV after gap coupling increase. Error bar shows standard deviation of changes. Gap coupling strength was increased by 200% for all gap junctions in the uniform case and it was increased by 400% for 50% of gap junctions in the nonuniform case.

3.3.4 Effective tissue conductivities

The changes in conduction velocity and AR were observed with changes in the microscopic parameters governing the cell shape, orientation and cleft density. One question of interest is how the changes in these parameters affected the macroscopic conductivities. As noted, the effective tissue conductivity was determined using the global, equivalent circuit method and the local, subthreshold response method (see Methods). In the global method, the membrane was removed leaving only the passive intracellular space and a current was delivered on one edge and grounded at the other edge such that the conductivities could be estimated using equation (3.3) and (3.4). In the local method, a subthreshold, intracellular stimulus was applied and the conductivities in both directions were estimated by first determining membrane resistance and then fitting the potential distribution to a continuous passive model. The conductivity estimation methods were first tested using a tissue with rectangular cells of length 120 μm and of width 24 μm for which an analytical solution exists. The methods were tested for three different gap conductances. Table 3.5 shows the results from the global and local estimation methods. Both methods match the analytical solution very well for the case of uniform tissue of rectangular cells in a regular lattice over the range of gap conductances studied.

Table 3.5: Tissue conductivity comparison from analytical method and numerical methods (global estimate and local estimate) in a tissue model of rectangular cells

σ_g	0.0167	0.167	1.67
LCV (cm/sec)	12.3	42.0	86.2
Analytical σ_L (mS/cm)	0.123	1.05	4.35
Global method σ_L (mS/cm)	0.123	1.05	4.35
Local method σ_L (mS/cm)	0.126	1.05	4.36
TCV (cm/sec)	6.37	20.3	55.6
Analytical σ_T (mS/cm)	0.0249	0.241	1.82
Global method σ_T (mS/cm)	0.0249	0.241	1.82
Local method σ_T (mS/cm)	0.0252	0.237	1.82

Two estimation methods were then applied to the discrete tissues, TC0 - TC4, and the result is shown in Figure 3.8. In the local method, the passive membrane resistance was estimated to be 9.66 $k\Omega \cdot cm^2$ and this value was used for all the tissues. Although there was some difference in the estimation, the correlation coefficients of two methods are 0.97 and 0.98 for longitudinal and transverse conductivities, respectively. The effective conductivities for the five models were estimated by the global method and are given in Table 3.6. The results show that both longitudinal and transverse conductivities are negatively correlated with the amount of cleft space.

Table 3.6: Effective conductivity obtained by global method

	TC0	TC1	TC2	TC3	TC4
σ_L	0.842 (4.2e-3)	0.767 (7.4e-3)	0.632 (7.1e-3)	0.474 (5.7e-3)	0.326 (1.2e-2)
σ_T	0.060 (5.3e-4)	0.046 (6.1e-4)	0.032 (5.0e-4)	0.021 (7.3e-4)	0.011 (1.1e-3)

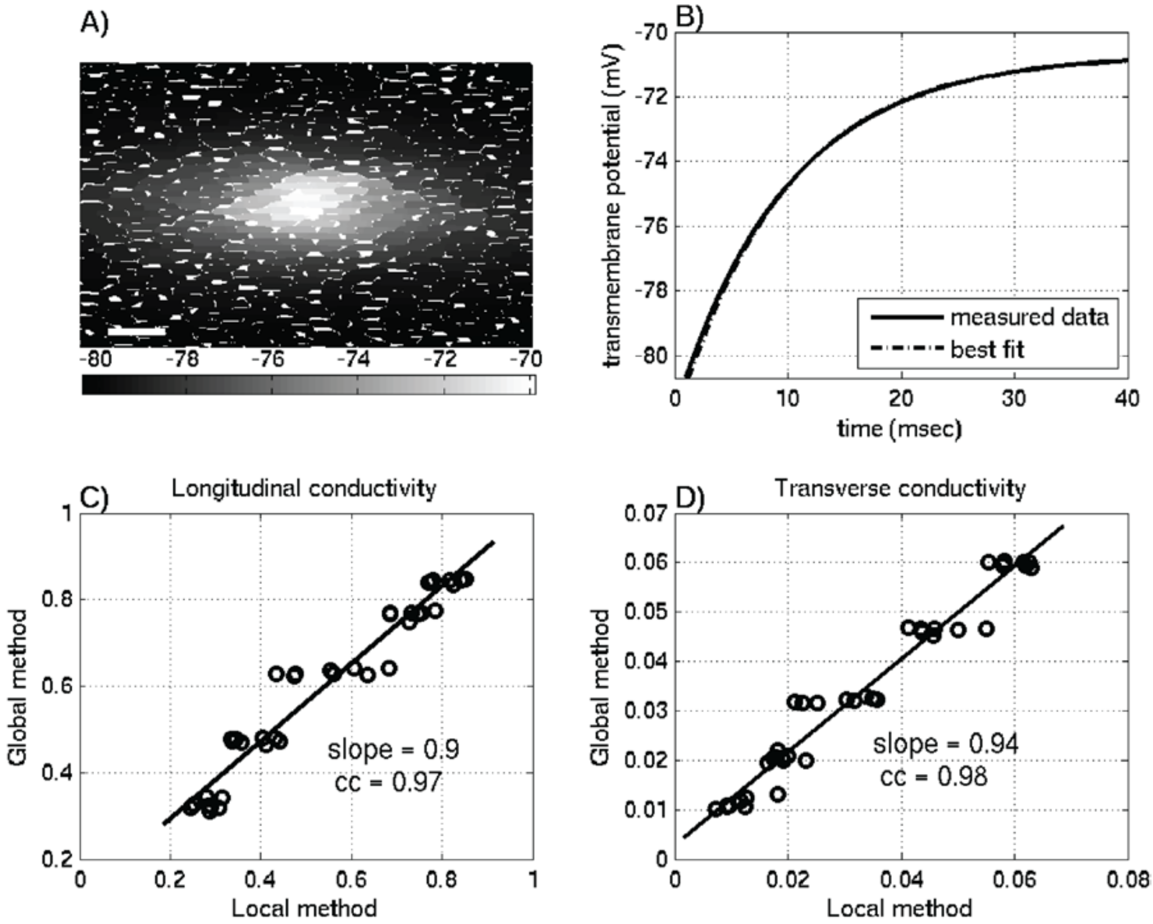

Figure 3.8: A) Steady state potential distribution by the subthreshold point stimulus. The scale bar is 200 μm. B) Time course of membrane potential at the center of the tissue and its best fit with estimate $R_m = 9.66 k\Omega \cdot cm^2$. C, D) Estimated effective tissue conductivity comparison between global method and local method for longitudinal and transverse directions. The solid line is the best fit. cc = correlation coefficient

The conductivity estimation methods were also compared in a tissue with an abrupt change in cell orientation. In this tissue, cells were aligned in the horizontal direction on the left half and in the vertical direction in the right half. The cleft probability was zero on both halves. Figure 3.9 A shows the estimated conductivities under the following scenarios: a) global method applied only to the left half of the tissue, b) local method applied to several sites along the tissue; c) global method applied to the entire tissue and d) global method applied only to the right half of the tissue. The estimates for cases a, c, and d are 0.85, 0.11 and 0.058, respectively. The results show that the local method estimates a relatively smooth change in conductivity across the transition site while the global method applied across the entire tissue nearly predicts an average conductivity of the two halve $\left(\left(0.5\left(\frac{1}{0.85}+\frac{1}{0.058}\right)\right)^{-1}=0.11\ mS/cm\right)$. It is important to note that the local method does a good job of estimating the conductivity away from the transition site in the right half of the tissue where the space constant is smaller than in the left half where the space constant in larger and the effect of the boundary on the flow of current is greater.

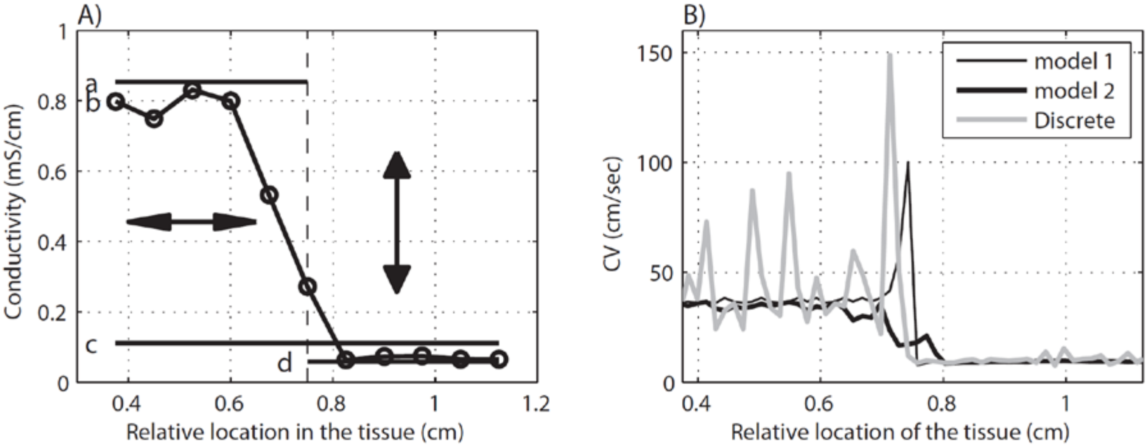

Figure 3.9: A) Changes in the estimated conductivity as a result of changes in cell orientations. The double headed arrows indicate the cell orientations. a. estimated conductivity by the global method applied to only the left half of the tissue. b. estimated conductivity by the local method. c. estimated conductivity by the global method for the whole tissue. d. estimated conductivity by the global method applied to only the right half of the tissue. B) CV changes of a wavefront moving from the left half of the tissue to the right half for the Discrete Model, the continuous model with conductivities based on the estimates from the local method (model 1), and a continuous model with the conductivities on the right and left halves based on the estimates from the global method (model 2).

3.3.5 Effective tissue conductivity and conduction velocity

The changes in macroscopic conductivities due to changes in the microstructure in the discrete tissues suggest that a continuous model with the same macroscopic conductivities could be used to explain the changes of CV seen in Figure 3.5. Table 3.6 gives the effective longitudinal and transverse conductivities of the five models. The inclusion of cleft space reduces not only the effective transverse conductivity, as expected, but also the longitudinal conductivity. The lateral uncoupling causes a slowdown in both the longitudinal and transverse conduction velocities as shown in Table 3.3. The effective conductivities for all realizations were then applied to continuous models. Figure 3.10 A shows that ratio of LCV's and TCV's in continuous and discrete models is close to 1 for all the tissues. Figure 3.10 B shows that when gap conductance tissues with clefts (TC1, TC2, TC3 and TC4) were increased uniformly such that the effective conductivities of those tissues were identical to those of the confluent tissue, TC0, the LCV's and TCV's were nearly the same. Finally, when the conductivity estimation method was repeated for all the tissues in Figure 3.5 whose CV varied with changes in cell length/width ratio, cell orientations and clefts, the square root of estimated conductivities was linear with CV (correlation efficient 0.995 (Figure 3.10 C)) as expected from continuous media theory.

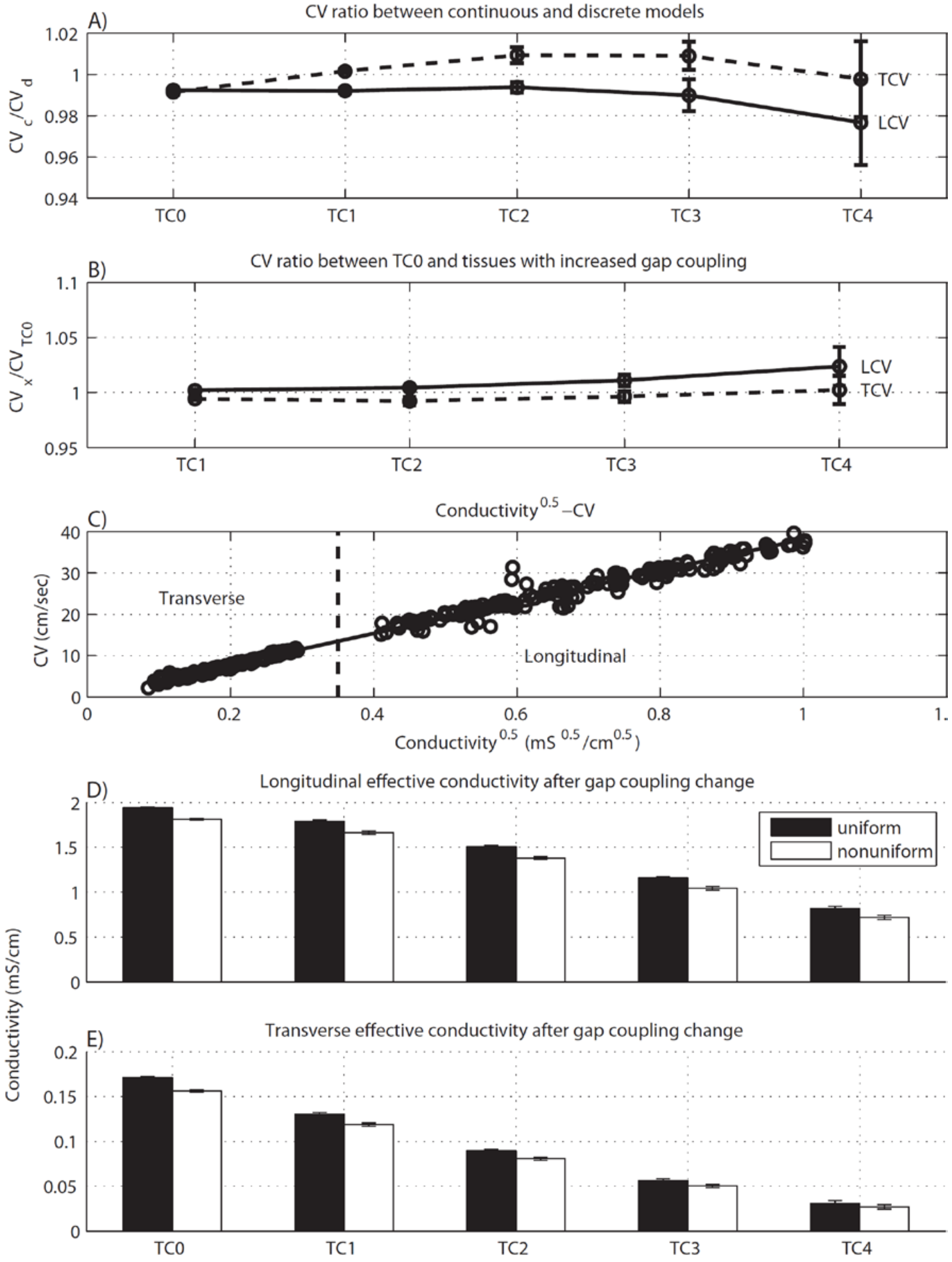
A)
CV ratio between continuous and discrete models
CV_c/CV_d
1.02
1
0.98
0.96
0.94
TCV
LCV
TC0
TC1
TC2
TC3
TC4
B)
CV ratio between TC0 and tissues with increased gap coupling
CV_x/CV_{TC0}
1.1
1.05
1
0.95
LCV
TCV
TC1
TC2
TC3
TC4
C)
Conductivity$^{0.5}$ –CV
CV (cm/sec)
40
30
20
10
0
Transverse
Longitudinal
0
0.2
0.4
0.6
0.8
1
1.
Conductivity$^{0.5}$ (mS$^{0.5}$/cm$^{0.5}$)
D)
Longitudinal effective conductivity after gap coupling change
2
1.5
1
0.5
0
uniform
nonuniform
Conductivity (mS/cm)
E)
Transverse effective conductivity after gap coupling change
0.2
0.15
0.1
0.05
0
TC0
TC1
TC2
TC3
TC4

Figure 3.10

Figure 3.10: A) CV ratio of the continuous model and the discrete model, whose passive conductivities are identical. B) CV ratio between TC0 tissue and tissues with increased gap coupling so that their passive conductivities are identical. C) CV vs. square root of conductivity for tissues shown in Figure 3.5. All data points are pooled together. Low CV points are from transverse propagation and high CV points are from longitudinal propagation. The line shows best linear fit with slope 38.0 and correlation coefficient 0.995. D) Longitudinal effective conductivity of tissues in Figure 3.7. E) Transverse effective conductivity of tissues in Figure 3.7

Finally, although the above results support the strong correlation between CV and the effective conductivity, the estimation of the conductivities for a continuous model is more challenging to interpret when the properties are not uniform. To investigate this, AP propagation was simulated in the domain with an abrupt change in cell orientation (Figure 3.9 A). The propagation velocities were plotted from the discrete model and from two continuous models. In one continuous model (model 1), the conductivities were assigned to the values obtained using the global, equivalent circuit method on each half separately. In the other continuous model (model 2), the conductivity was assigned to be smoothly varying based on the estimates obtained using the local, subthreshold response method. When the AP was initiated from left edge of the tissue, both model 1 and the discrete model showed an abrupt increase in CV near the transition of the change in cell orientation before the CV decreased. In model 2, the CV gradually slowed without an abrupt CV increase (Figure 3.9 B). Thus while the local measurements suggested a smooth change in conductivities, using such tissue properties does not yield behavior that is seen in tissue with an abrupt change in cell orientation. Note that although it appears that the CV fluctuations are larger on the left half of the tissue than on the right (Figure 3.9 B), a closer examination shows that the size of the fluctuations relative to the average conduction velocity is approximately the same.

3.4 Discussion

In this chapter, we present a new methodology to develop models of cardiac tissue structure that more closely replicates the complex and arbitrary cell shape and orientations found in engineered monolayers. The technique can also be applied to diseased regions like an infarct scar where there can be significant heterogeneity and sparse, disorganized cell structure (Gardner, Ursell et al. 1985; Cabo and Boyden 2003). Because it is straightforward to create different tissue realizations with the same statistical properties, it is possible to perform simulations in a manner consistent with experimental studies where several tissue or heart preparations are used.

One of the key questions addressed in this study is how conduction is influenced by cell orientation and degree of cleft space corresponding mostly to transverse decoupling. Bursac et al. showed that by decreasing the degree of background fibronectin concentration between the micropatterned fibronectin lines, the cells are increasingly elongated and oriented along the lines (Bursac, Parker et al. 2002). This results in an increase in longitudinal conduction velocity, a decrease in transverse conduction velocity, and an overall increase in anisotropy ratio of the conduction velocity. As the background fibronectin concentration is further decreased, the longitudinal intercellular clefts start to form followed by the increase in their length and number. This results in a further decrease of transverse conduction velocity along with a slow decrease in longitudinal velocity, which overall yields a further increase in the conduction velocity anisotropy. This increase in structural discontinuity results in a decrease in longitudinal conduction velocity (for AR > 3.4), a decrease in transverse conduction velocity, and an overall increase in anisotropy ratio. As shown in Figure 3.5, the simulated results were consistent with these experimental findings as the modeling methodology allows for arbitrarily oriented cells as well as aligned cells with differing amounts of cleft space. The simulated results also show that AR for which there is a decrease in longitudinal conduction velocity increases with increasing cell-length to width ratio.

The results also revealed that in the monolayer, longitudinal conduction velocity can be slowed when there is transverse decoupling. In a previous modeling study, Hubbard and Henriquez showed that in a regular cell structure with no cell overlap, transverse decoupling has no effect on longitudinal conduction (Hubbard, Ying et al. 2007). In contrast, in a brick wall structure with cell overlap, longitudinal conduction is facilitated by the transverse connections. As a result, a loss of transverse coupling reduces velocity as seen in the monolayers.

One of the distinct advantages of the computational model is the ability to compute or estimate the effective tissue electrical properties associated with the various tissue structures. Using a global estimation method, we show (Figure 3.10 C and Table 3.6) that the decrease in longitudinal conduction velocity with transverse decoupling is also associated with a decrease in the effective longitudinal conductivity. In other words, the overlap of cells acts to effectively increase the effective longitudinal conductivity and explains the increase in LCV seen by Hubbard and Henriquez (Hubbard, Ying et al. 2007) in brick wall models. Because of the ability to consider several realizations of a given tissue, it is possible to obtain statistics regarding the estimates. In general, the greater the degree of transverse decoupling, the greater the variance in the estimates of the effective conductivity (Table 3.6), demonstrating the effects of small perturbations in microscopic structure on the current flow.

The simulations also showed that the distribution of the coupling strength can affect the conduction velocity. A global uniform increase in gap junction conductance did not lead to the same conduction velocity as did a non-uniform increase in gap junction conductance, even though the average conductance change was the same in both cases. The results showed that the non-uniform gap coupling increase (118% longitudinal and 158% transverse increase in effective conductivity) led to a lower effective conductivity than that resulting from a uniform increase in gap coupling (139% longitudinal and 187% transverse increase in effective conductivity) (Figure 3.10 D and E), and hence a lower conduction velocity (Figure 3.7). While this appears to be surprising, the result is actually expected if the cells are considered as connected in series. Because the gap junctions are in series, the increase in conductance, C, leads to a decrease in resistance R. For two gap conductances of strength C, the total resistance is $R = 1/C + 1/C = 2/C$). If the total gap conductance is uniformly doubled from 2C to 4C, the total resistance is halved (R = 1/2C +1/2C = 1/C). If, however, one conductance is unchanged and the other the tripled such that the total conductance is again doubled to 4C, the effective resistance is larger than in the uniform case (R = 1/C +1/3C = 4/3C). In the monolayer, the way in which the conductances sum is more complicated and hence it is not always obvious how a certain distribution of gap junctions will impact the electrical properties. This study shows that the global method properly estimates the changes in conductivity that explains the changes in conduction velocity.

Under the conditions studied, the changes in velocity associated with cell size, orientation and the distribution and strength of coupling comprising the highly discrete structure could be explained by the corresponding changes in the effective conductivities. Because tissue conductivities require a model to interpret the measurements, two methods were used to determine the values. The first method, which is not applicable under experimental conditions, removed the membrane elements in the model, applied a current through the intracellular space and evaluated the potential. The effective conductivity is obtained through an estimate of the electric field and the use of equation (3.4). Because the field is applied across the entire tissue, the estimate is an effective global conductivity. The values arising from this method were verified using a simplified tissue structure for which an analytical solution was available. The second method may be experimentally realizable as it uses a subthreshold stimulus response of the tissue, and applies a parameter estimation method with a continuous model to determine the effective conductivities. Both estimation methods agreed very well with the analytical solution for the case of regular, rectangular cells (Table 3.5). Although some small differences were found between the two methods for the discrete tissue with nearly uniform cell orientations and clefts, the estimated conductivities from the two methods showed strong correlation.

The local estimation method did not perform as well with abrupt change in cell orientations (Figure 3.9 A). The local measurement estimates that the conductivity smoothly varies at the transition site. When the smooth conductivities were applied to a continuous model, the resulting conduction velocities and action potential upstrokes near the transition site did not agree with those obtained in the discrete model, as shown in Figure 3.9 B. In the discrete model, the CV sharply increased as the wavefront moved from the longitudinally oriented cells to the transversely oriented cells. Note that an abrupt decrease in CV occurred in both the continuous model with abrupt changes in conductivity and the discrete tissue but not in the continuous model with a smooth change in conductivity and when the wavefront moved in the opposite direction (not shown). This abrupt increase in CV by conductivity changes can be explained by the current-to-load concept; as the wavefronts approaches the boundary, less current flows in the neighboring tissue due to the lower conductivity and the conduction accelerates (Wang and Rudy 2000). Figure 3.9 B also shows that the continuous model with abrupt changes in the properties better predicted the behavior of the discrete network. These results suggest that care must be taken when estimating properties in regions with abrupt transitions in fiber orientation or discreteness; particularly when using these estimates to construct a continuous model. Note that while the local method may be experimentally realizable, it requires a measurement of the absolute potential distribution over a large area. While optical methods can be used to assess the distribution, the measurements only reflect relative changes. One approach to overcome this limitation is to calibrate the optical mapping measurements with one microelectrode measured data which was shown by Pastore et al (Pastore, Girouard et al. 1999).

While the new approach for modeling discrete tissues was able to simulate some phenomena observed in monolayers, a few limitations remain. First, the choice to use cells with relatively fixed geometries led to the emergence of holes in the domain when the cell orientations were random. Such holes are not observed in confluent monolayers, because the cells will spread to fill in the holes (Bursac, Parker et al. 2002). In addition, the clefts in the model were generated by shrinking cells laterally, while the clefts *in vitro* result from insufficient expansion of the cells. The model is capable of generating any cell shape but the ability to create random networks automatically required some compromises. Future studies will consider greater flexibility in the assignment of cell shapes and a tissue generation algorithm that more closely mimics the variety of cell shapes seen in engineered monolayers. It is important to point out that because we assumed a monodomain, the model does not fully account for the effects of tight spaces on conduction (Roberts, Stinstra et al. 2008). The Bueno-Orovio-Cherry-Fenton-Karma model rather than a detailed ionic-based membrane model was used to reduce the time of the simulations and to consider it usefulness when performing estimation with experimental data. While the Bueno-Orovio-Cherry-Fenton-Karma model can reproduce many of the features seen in Hodgkin-Huxley type membrane models, the lack of true ionic currents may limit its utility under some critical regimes of conduction. Note for the studies considered here of a single wavefront, the difference between the Bueno-Orovio-Cherry-Fenton-Karma model and more detailed model is expected to be small. Finally, the studies performed here and the conclusions derived from the simulations are based on cells with neonatal distributions of gap junctions. More work is needed to determine how the conclusions generalize to tissues with adult cell shapes and distributions of gap junctions. The method, however, can easily be extended to such cases with no modification.

4. Effective intracellular conductivity estimation

4.1 Introduction

A cultured cardiac monolayer tissue is a useful experimental model to study initiation and development of arrhythmias since 1) the discrete features of the tissue such as cell orientations and distributions of clefts can be controlled, 2) the impulse propagation can be observed conveniently by the optical mapping and 3) a corresponding computer model can be built, using the approach described in Chapter 2, to develop further insights into the mechanisms of conduction failure (Entcheva, Lu et al. 2000). The computer model also allows fine control over many parameters and thus enables investigations that are difficult if not impossible under the experimental conditions (Henriquez 1993; Sampson and Henriquez 2002; Rudy and Silva 2006). However, building a predictive computer model for the tissue preparation often requires that a set of model parameters to be determined from experimental observations. The computational cardiac model has two primary features: the passive electrical properties and the membrane properties. The passive tissue properties are the effective continuous intracellular and extracellular conductivities, while the membrane properties are determined by the ion channel dynamics of the cell. While the ion channel model is built by analyzing single cell recordings, the conductivities of the tissue are usually assigned to match the observed action potential (AP) conduction velocity. This method can determine the proper tissue conductivities only when the correct ion channel model is available. However the ion channel model is not available in many cases and the tissue conductivities are usually assigned as physiologically reasonable values so that the behaviors of the model and experimental observations are similar.

Several groups have developed methods to determine the tissue conductivities in which a specific model is used to interpret potential measurements. The four electrode method by Plonsey and Barr uses a linear array of four equally spaced electrodes to estimate bidomain model parameters and this method is limited to the tissue with equal anisotropy ratios (Plonsey and Barr 1982). This method has been extended to eliminate an equal anisotropy ratio requirement and to handle the alignment between the fiber and the electrode by using multiple electrodes or high frequency stimulus with numerical method for data fitting (Le Guyader, Trelles et al. 2001; Pollard and Barr 2006; Sadleir and Henriquez 2006). On the other hand, there are few studies to estimate the monodomain model parameters. Fast and Kleber used optical mapping data for estimating intracellular conductivity and gap coupling for one dimensional discrete fiber model (Fast and Kleber 1993).

In this study, we developed a method to estimate the effective intracellular conductivities (EICs) of an *in vitro* monolayer of tissue. The estimated values are compared to the conductivities calculated from the equivalent circuit model (see Chapter 3) representing the intracellular domain. The method approximated membrane resistance under subthreshold stimulus as a second order polynomial of membrane potential and this polynomial and the EICs were estimated from spatiotemporal pattern of the optical mapping. This simplified membrane model allowed us to estimate the EICs relatively accurately without the detailed knowledge of the membrane properties.

4.2 Methods

4.2.1 Surrogate data

To generate data, the discrete monolayer tissue model was used instead of a cultured tissue. For the membrane dynamics in the surrogate tissue, the Pandit model and Luo-Rudy model were used (Luo and Rudy 1991; Pandit, Clark et al. 2001). The membrane potential was computed and used as if it was recorded using microelectrode or via optical mapping. The microelectrode recording was simulated by averaging the membrane potential over a cell. In order to simulate the optical mapping, circular optical sensors were assumed with a fixed radius and location. At each time step of the simulation, the membrane potential was spatially averaged under each sensor and this averaged membrane potential was used as the “measured” data. After the simulation was over, these recorded values were shifted and normalized so that the maximum of the recordings is 1 and the minimum of the recordings is 0. Three surrogate tissues were generated with different gap coupling strength and the effective intracellular conductivities of the tissues were obtained from the global method (Table 4.1) described in Chapter 3 in which the membrane elements were removed. The effective intracellular conductivities (EICs) from the global method were considered as the true conductivities of the corresponding tissues and compared with the values from the estimation method.

Table 4.1: Longitudinal and transverse EICs and their ratio of the discrete tissue

Gap coupling strength	Longitudinal conductivity	Transverse conductivity	Ratio
4 mS/cm	4.58 mS/cm	0.94 mS/cm	4.87
1 mS/cm	2.78 mS/cm	0.31 mS/cm	8.97
0.25 mS/cm	1.10 mS/cm	0.084 mS/cm	13.10

4.2.2 Estimating membrane resistance from a single cell

The time response of the single cell's membrane potential under subthreshold stimulus was modeled as a simple RC circuit while the specific membrane capacitance was assumed to be 1 $\mu F/cm^2$. The subthreshold membrane response can be divided into depolarization phase and repolarization phase as shown in Figure 4.1 and three different membrane resistances were obtained depending on which part of the membrane potential was used for the estimation.

1) Depolarization: The normalized membrane potential from onset of the stimulus can be modeled as $V_m = 1 - \exp\left(-\frac{t}{R_m C_m}\right)$. This analytical expression was compared to normalized membrane potential during depolarization and the membrane resistance R_m was found by an optimization process. This membrane resistance is heretofore referred to as R_{m1}.

2) Repolarization: After the stimulus was removed, the normalized membrane potential can be modeled as $V_m = \exp\left(-\frac{t}{R_m C_m}\right)$. This analytical expression was compared to normalized membrane potential during repolarization and the membrane resistance R_m can be found by an optimization process. This membrane resistance is heretofore referred to as R_{m2}.
3) Combined: Both depolarization and repolarization of membrane potential were compared to corresponding analytical expressions and the membrane resistance R_m was optimized for both depolarization and repolarization membrane potential. This membrane resistance is heretofore referred to as R_{m3}.

In addition to these methods, a transient membrane resistance was evaluated by $R_m = \frac{(V_m + dv) - (V_m - dv)}{I_m(V_m + dv) - I_m(V_m - dv)}$ and this is heretofore referred to as R_{m4} (Sampson and Henriquez 2005). Note that the relationship between the steady state membrane potential change and the membrane resistance, $\Delta V_m = I_{stim} R_m$, is not used to estimate membrane resistance because of the uncertainty regarding the membrane area in the experimental conditions.

4.2.3 Estimating effective intracellular conductivities with simplified membrane model

We assumed an EIC for both the longitudinal and transverse directions and modeled the membrane resistance as a second order polynomial of membrane potential in the following form.

$$R_m = A \cdot (V_m - B)^2 + C \tag{4.1}$$

where V_m is the membrane potential and A, B, and C are parameters of the polynomial to be estimated from the experimental data. The EICs and membrane resistance were estimated from spatiotemporal response of two dimensional tissues for the subthreshold stimulus. A two dimensional tissue was stimulated with two subthreshold stimulus patterns in longitudinal and transverse directions with a planar electrode. The stimulus was 200 – 300 msec long and the membrane potential reached steady state at the end of stimuli. The stimulus strength was controlled so that the maximum depolarization was from 10 to 15 mV. The membrane potential was recorded with the optical mapping and the EICs and the polynomial modeling the membrane resistance were obtained by minimizing the difference in the depolarization patterns between recorded tissue responses and those of the simulated continuous tissue model.

4.2.4 Simulation and estimation detail

The monolayer tissue was implemented with the monodomain model following the method in the previous chapter. The size of the tissue was 7 mm by 4 mm for all cases. Three tissues were considered with different gap coupling strength: 4 mS/cm, 1 mS/cm, and 0.25 mS/cm. The system of equations was solved using the Crank-Nicolson method with a time step size 10 μsec (Keener and Bogar 1998). During the optimization, the domain size of the continuous tissue model was represented as a strip of tissue to reduce the computational time. For the longitudinal stimulus, the size of the continuous tissue was 7 mm by 0.4 mm. For the transverse stimulus, the size of the continuous tissue was 0.4 mm by 4 mm. This reduction in the tissue size was found not to affect the parameter estimation. The optical mapping recordings were simulated to investigate how the number and radius of the sensors affected the estimation. The radii of the sensors were 45 μm, 90 μm and 180 μm while the numbers of sensors were 16, 32, and 64 for longitudinal direction and 8, 16 and 32 for transverse direction. The differential evolution algorithm was used (Storn and Price 1997) to perform the estimation. The differential evolution algorithm has been shown to find the global minimum of a multidimensional function with good probability. The error function for the optimization was defined as squared sum of the error in the following form.

$$E = \frac{1}{2}\sum_{t}\sum_{i}\left(OP_{data}(t,i) - OP_{sim}(t,i;x)\right)^2 \tag{4.2}$$

where $OP_{data}(t,i)$ is optical mapping data from the sensor i at time t and $OP_{sim}(t,i)$ is simulated optical mapping from the sensor i at time t. x is a vector of parameters to be estimated. As the differential evolution algorithm parameter, the crossover rate was set as 0.9 and the weighting factor F was randomly selected between 0.5 and 1.0 at every generation. The number of population was 12.

4.3 Results

4.3.1 The passive membrane resistance estimation from RC circuit analysis

The membrane resistance was estimated by RC circuit analysis while the cell was stimulated with subthreshold pulse. Figure 4.1 A compares optical mapping and ideal RC circuit response with resistance values estimated from different part of the waveform. In this Figure, R_{m1} fits best during the depolarization, R_{m2} fits best during the repolarization and R_{m3} stays between R_{m1} and R_{m2}. Figure 4.1 B shows the transient membrane resistance R_{m4} for Figure 4.1 A. The membrane resistance increases and then decreases during the pulse.

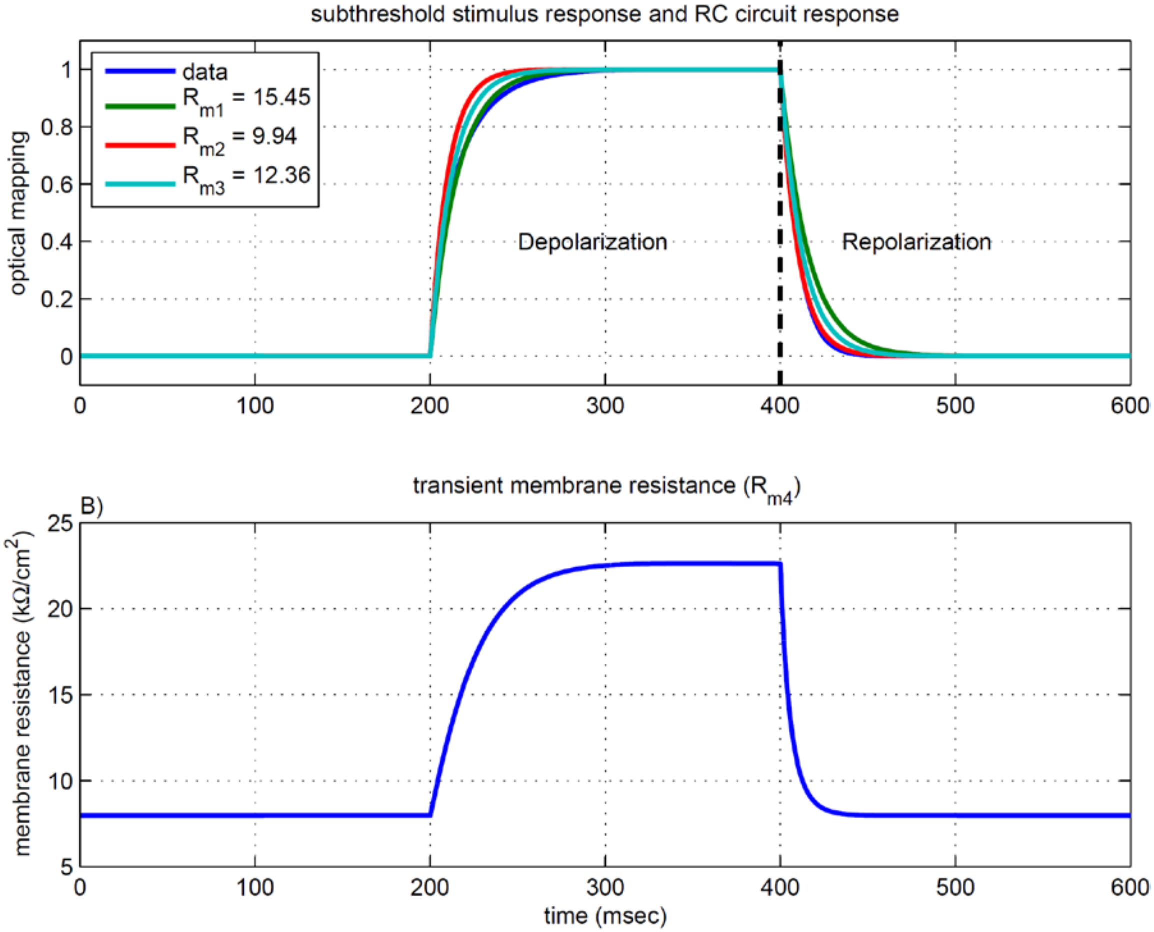

Figure 4.1: A) Comparison between optical mapping of Pandit model when subthreshold stimulus was applied and response of the equivalent RC circuit with different membrane resistances. R_{m1} showed the best fit during depolarization while R_{m2} showed the best fit during repolarization. B) Transient membrane resistance R_{m4} during subthreshold stimulus. The overall shape of membrane resistance follows that of membrane potential.

4.3.2 The effective intracellular conductivities with constant membrane resistance

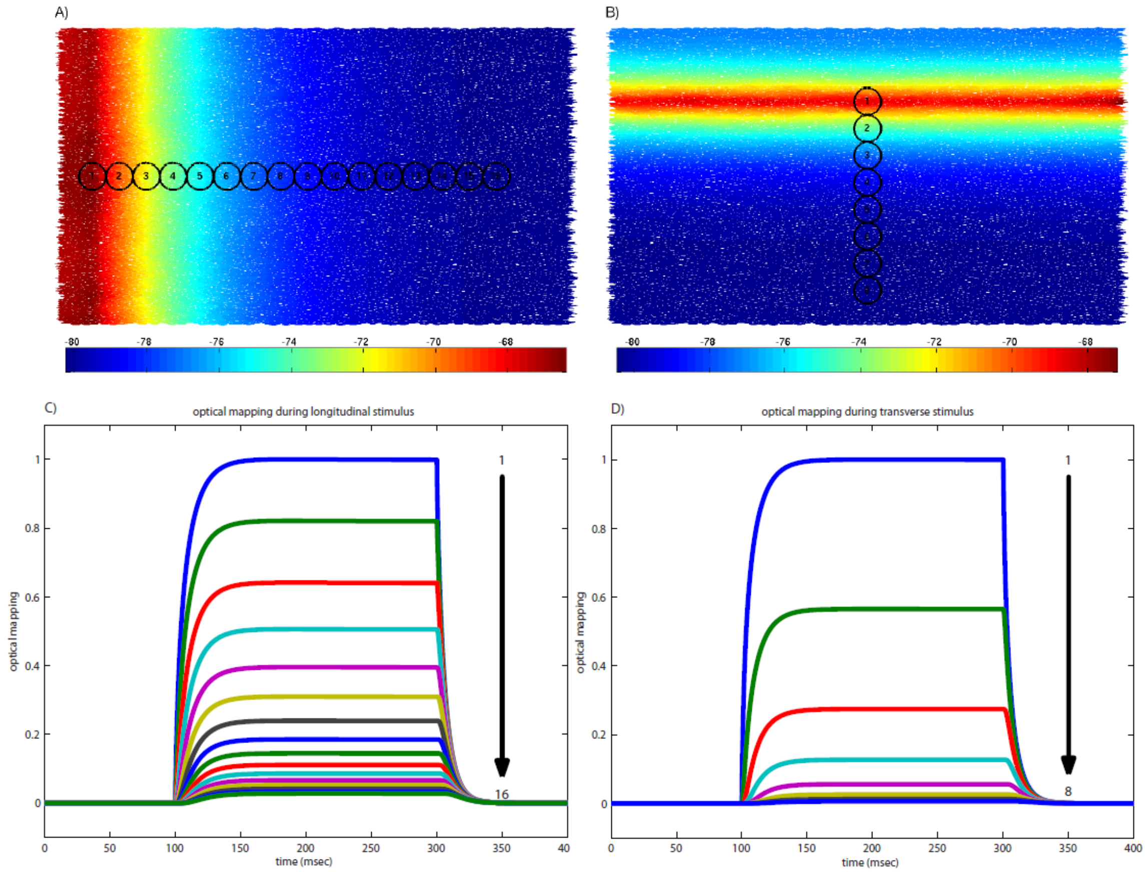

Figure 4.2: A, B) Membrane potential distribution of Pandit model at the steady state when the subthreshold stimulus was applied in longitudinal and transverse direction. The circles indicate the location of optical sensors of radius 180 μm. The size of the tissue is 7mm by 4 mm. C, D) Optical mapping measured from the sensors in A) and B). The arrow on the right indicates the sensor number. Because of the normalization, the maximum of optical mapping is 1 and the minimum of the optical mapping is 0.

Figure 4.2 A and B show the potential distribution at the steady state in the domain for stimulation in the longitudinal and transverse directions, respectively. Figure 4.2 C shows the optical mapping recorded at different sensor locations shown in

Figure 4.2 A and Figure 4.2 D shows the optical mapping at the different locations shown in Figure 4.2 B. Because the true voltage will not be measured, the simulated optical mapping data was normalized such that the signal has maximum of 1 and a minimum of 0. If the membrane resistance can be considered as a constant, the EICs can be estimated by using only the steady state membrane potential distribution. Although the membrane resistance was found to be different for the rising and falling phases, studies were performed to determine if a fixed membrane could be used to perform the estimations. Initial studies showed that estimated values had a tendency to diverge when only longitudinal and transverse stimulus patterns were given as data. The divergence in the estimation was prevented by providing a point stimulus pattern as additional data. As a result, this method used three stimulus patterns: longitudinal, transverse and point stimulus patterns. Although additional data was provided to improve the performance, consistently good estimations of the EICs still could not be achieved with the constant membrane resistance. The tables 4.2 and 4.3 summarize the percentage error of the estimated EICs and their ratios compared to the values from the global method for Pandit model and Luo-Rudy model, respectively with a fixed membrane resistance. The error E is calculated by $E = \frac{C_e - C_g}{C_g} \times 100$ where C_e is estimated EIC and C_g is EIC from the global method. From this definition of the error, an overestimation results in the positive error and an underestimation results in the negative error. Table 4.2 and 4.3 show that when the number of sensors is the same, the estimated value tends to increase as the size of the sensor decreases. Increasing the number of sensors did not improve the estimation accuracy but it decreased the estimations both in Pandit model and in Luo-Rudy model. Although the estimated EICs from this method were not quite accurate, the ratios of the conductivities had relatively lower error.

Table 4.2: Percentage error of EIC estimates with constant membrane resistance for Pandit model. The constant membrane resistance was 12.58 $k\Omega cm^2$. The values in parenthesis are the number of sensors in longitudinal and transverse direction.

	45 μm (16,8)	45 μm (64,32)	90 μm (16,8)	90 μm (32,16)	180 μm (16,8)
			Longitudinal		
4 mS/cm	-12.88	-20.67	-17.37	-20.26	-23.70
1 mS/cm	-14.18	-20.00	-16.99	-19.08	-23.06
0.25 mS/cm	-20.98	-23.11	-20.47	-20.84	-24.59
			Transverse		
4 mS/cm	-7.31	-17.78	-18.26	-19.84	-25.01
1 mS/cm	-8.93	-14.09	-18.26	-18.70	-25.06
0.25 mS/cm	-10.73	-11.86	-16.68	-16.71	-24.40
			Ratio		
4 mS/cm	-6.01	-3.51	1.10	-0.52	1.75
1 mS/cm	-5.77	-6.88	1.56	-0.47	2.67
0.25 mS/cm	-11.45	-12.77	-4.54	-4.95	-0.26

Table 4.3: Percentage error of EIC estimates with constant membrane resistance for Luo-Rudy model. The constant membrane resistance was 6.29 $k\Omega cm^2$. The values in parenthesis are the number of sensors in longitudinal and transverse direction.

	45 μm (16,8)	45 μm (64,32)	90 μm (16,8)	90 μm (32,16)	180 μm (16,8)
			Longitudinal		
4 mS/cm	-27.35	-32.72	-30.91	-32.11	-35.98
1 mS/cm	-28.62	-32.15	-30.70	-31.23	-35.44
0.25 mS/cm	-29.91	-31.28	-30.62	-30.67	-35.20
			Transverse		
4 mS/cm	-21.35	-23.24	-31.35	-32.07	-36.99
1 mS/cm	-19.81	-20.97	-30.33	-30.43	-36.44
0.25 mS/cm	-19.62	-20.02	-27.83	-27.83	-36.00
			Ratio		
4 mS/cm	-7.63	-12.35	0.65	-0.06	1.61
1 mS/cm	-10.99	-14.14	-0.52	-1.15	1.58
0.25 mS/cm	-12.81	-14.08	-3.87	-3.93	1.25

4.3.3 The membrane resistance as a function of membrane potential

Figure 4.1 showed that there is some difference between the membrane potential and the RC circuit response and the membrane resistance was different for the depolarization and repolarization phases. As shown in Figure 4.3, the membrane resistance during each phase also varies as a function of membrane potential resulting from different stimulus amplitudes. This figure suggests that the membrane resistance under subthreshold stimulus can be better represented with a low order polynomial rather than as a constant. In order to avoid over-fitting, a second order polynomial was found to be a reasonable estimate (equation 4.1). The coefficients used in Figure 4.3 are summarized in the Table 4.4.

Table 4.4: The second order polynomial coefficient for membrane resistance during subthreshold stimulus

	Pandit model			Luo-Rudy model		
	A	B	C	A	B	C
R_{m1}	0.0358	-2.6046	7.945	0.0692	2.7413	4.3993
R_{m2}	0.0028	-22.9666	6.4571	0.0038	-8.6687	3.1486
R_{m3}	0.0146	-6.4808	7.4122	0.0232	0.3772	3.7865
R_{m4}	0.1220	1.1104	8.9846	0.1730	4.0249	5.0025

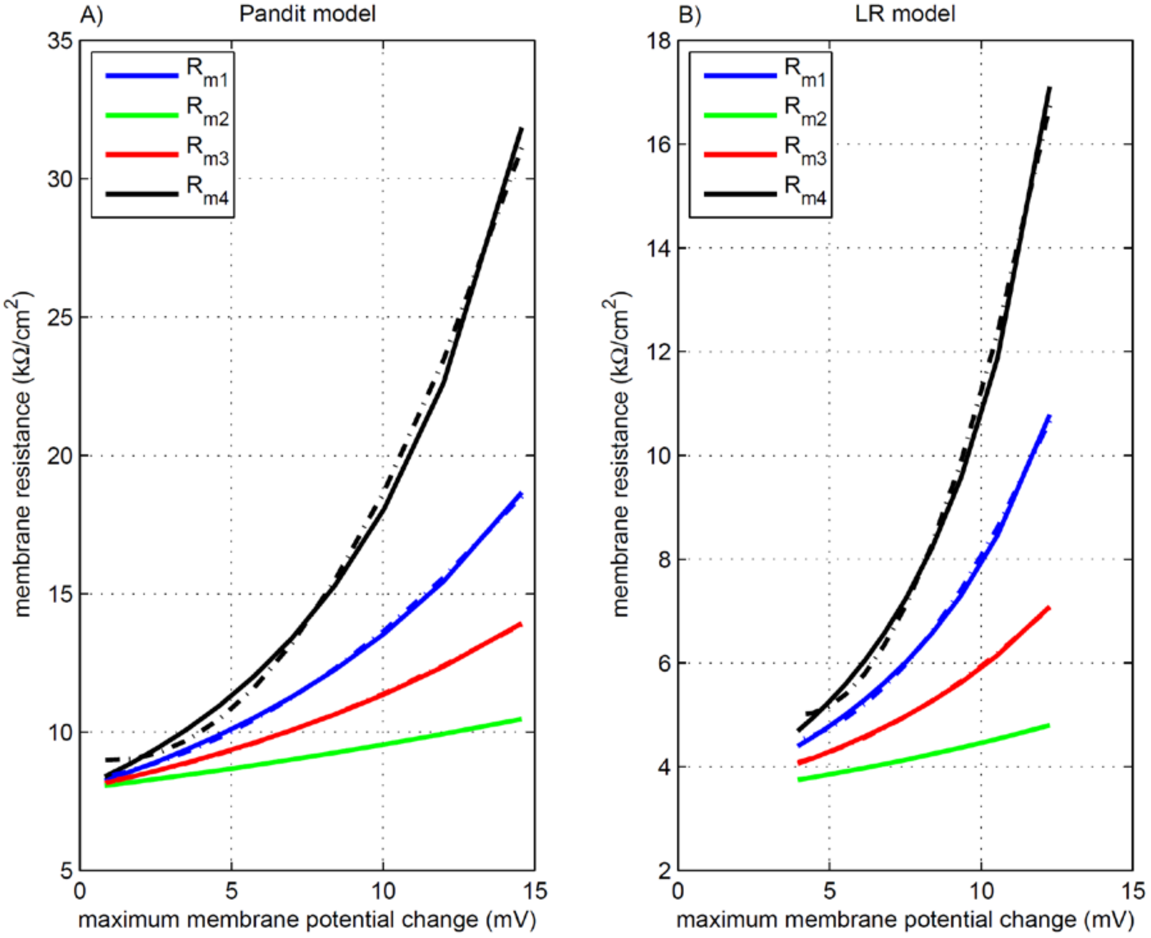

Figure 4.3: Membrane resistance as a function of maximum membrane potential change. The dotted lines show the best fit with a second order polynomial. In both Pandit model and Luo-Rudy model, the membrane resistance during subthreshold stimulus can be well approximated as a second order polynomial of the membrane potential (dashed dot lines).

4.3.4 The effective intracellular conductivities with simplified membrane model

Given the findings that membrane resistance varies as a function of membrane potential under subthreshold conditions, a new estimation scheme was developed in which the parameters of this polynomial and the EICs were estimated simultaneously from the spatiotemporal response of the tissue. This method requires significantly longer computation time compared to the method using constant membrane resistance since the full time response needed to be simulated at each iteration of the estimation. However, the new estimation scheme yielded EICs that were much more accurate. As shown in Table 4.5 and 4.6, the overall errors are below 10% for all the cases and do not show significant change due to the number or size of sensors for both membrane types. The Table 4.7 shows averages and standard deviations of the estimated coefficients of the simplified membrane function in the equation (4.1). The coefficients of the equation (4.1) were estimated at the same time with the EICs for the Table 4.5 and 4.6 and then these function coefficients were averaged over the number of sensors to obtain the values in the Table 4.7. The values in Table 4.7 are consistent with the values in Table 4.4 that were obtained from the single cell.

Table 4.5: Percentage error of EIC estimates for the Pandit model. The membrane resistance was approximated with a second order polynomial and the parameters of this polynomial were estimated with EICs. The values in the parenthesis are the number of sensors in longitudinal and transverse direction.

	45 μm (16,8)	45 μm (64,32)	90 μm (16,8)	90 μm (32,16)	180 μm (16,8)
			Longitudinal		
4 mS/cm	8.79	7.97	6.97	6.51	6.51
1 mS/cm	7.04	7.07	6.70	5.94	6.95
0.25 mS/cm	1.96	2.48	0.73	0.95	3.46
			Transverse		
4 mS/cm	2.22	5.57	5.17	5.12	6.32
1 mS/cm	3.20	5.19	4.89	5.03	6.36
0.25 mS/cm	-0.63	0.002	0.64	0.44	2.45
			Ratio		
4 mS/cm	6.43	2.27	1.71	1.32	0.17
1 mS/cm	3.72	1.79	1.72	0.86	0.56
0.25 mS/cm	2.61	2.47	0.09	0.51	0.98

Table 4.6: Percentage error of EIC estimates for the Luo-Rudy model. The membrane resistance was approximated with a second order polynomial and the parameters of this polynomial were estimated with EICs. The values in the parenthesis are the number of sensors in longitudinal and transverse direction.

	45 μm (16,8)	45 μm (64,32)	90 μm (16,8)	90 μm (32,16)	180 μm (16,8)
			Longitudinal		
4 mS/cm	8.63	8.51	4.26	2.92	5.42
1 mS/cm	6.95	4.55	3.43	4.14	2.33
0.25 mS/cm	5.79	5.74	1.17	1.05	2.54
			Transverse		
4 mS/cm	1.79	2.94	-0.13	-0.62	2.95
1 mS/cm	1.79	-1.93	-1.51	-0.41	-1.19
0.25 mS/cm	1.95	-1.49	-5.40	-5.02	-2.11
			Ratio		
4 mS/cm	6.72	5.42	4.39	3.56	2.40
1 mS/cm	5.07	6.61	5.02	4.57	3.56
0.25 mS/cm	3.77	7.34	6.94	6.39	4.75

Table 4.7: Averages of the simplified membrane model coefficient in the equation (4.1). The values in parentheses are the standard deviations. The coefficients of the equation (4.1) were estimated at the same time with the EIC estimates for the Table 4.5 and 4.6 and then these function coefficients were averaged over the number of sensors to obtain values in this table.

	A	B	C
		Pandit model	
4 mS/cm	0.016 (8.45e-4)	-3.505 (0.584)	8.038 (0.121)
1 mS/cm	0.023 (4.50e-3)	-0.658 (1.583)	8.440 (0.256)
0.25 mS/cm	0.035 (7.10e-3)	1.371 (1.172)	8.658 (0.129)
		Luo-Rudy model	
4 mS/cm	0.021 (3.84e-3)	-0.064 (1.053)	3.556 (0.135)
1 mS/cm	0.026 (4.34e-3)	1.088 (1.005)	3.650 (0.105)
0.25 mS/cm	0.026 (3.54e-3)	0.582 (1.010)	3.502 (0.156)

4.4 Discussion

In this chapter, we developed a method to estimate EICs from optical mapping of membrane potential while the tissue was stimulated by subthreshold pulse. It is generally assumed that under subthreshold conditions, the membrane resistance is constant. Under this assumption, the steady state membrane potential falls exponentially from the stimulus site. The rate of the fall in the potential is known as the tissue space constant, λ.

$$\lambda = A \cdot \sqrt{R_m C_i} \tag{4.3}$$

$$C_i = \frac{\lambda^2}{A^2 R_m} \tag{4.4}$$

where A is a constant determined by the geometry of the tissue and C_i is the EIC. Thus if the space constant can be measured from the membrane potential distribution and the exact membrane resistance is known, the EIC can be easily found from equation (4.4). However the membrane resistance is not constant as the subthreshold stimulus was applied but varies as a function of membrane potential. As shown in this study, when the membrane resistance is assumed to be constant, accurate EIC estimate cannot be obtained using simulated optical recordings. In general, the average estimation errors for the Pandit model are 19.9% and 16.9% for longitudinal and transverse EIC, respectively while the average estimation errors for the Luo-Rudy model are 31.7% and 27.6% for longitudinal and transverse EIC, respectively. In addition to this, when R_{m1}, R_{m2} and R_{m3} were used as a constant membrane resistance for the EIC estimation, the multiplication of estimated EIC and the membrane resistance was constant regardless of the membrane resistance and the membrane type (data not shown). This confirms that the stimulus pattern follows that of the one dimensional fiber and the relationship between the EIC and the membrane resistance can be expressed by the equation (4.4).

In the new method presented here, the estimates were significantly improved by using a simplified membrane model, which expresses the membrane resistance under subthreshold stimulus as a second order polynomial of membrane potential. By using this simplified form of membrane resistance, the average estimation errors for the Pandit model are 5.3%, 3.5% for longitudinal and transverse EIC, respectively while the average estimation errors for the Luo-Rudy model are 4.5% and 0.6% for longitudinal and transverse EIC, respectively. Additionally, the estimated coefficients of the simplified membrane in Table 4.7 model are consistent with the values in Table 4.4 that were obtained from the patch clamp recording. This supports the findings that the estimated coefficients of the equation (4.1) are not just a set of numbers minimizing the error function but, after the optimization process, they make the simplified membrane model physiologically meaningful.

While the approach gives reasonable estimate, there are several areas for improvement, the method was developed and tested with only surrogate tissue data generated by the monodomain model in which extracellular conductivities are infinite and the extracellular potential is grounded. The method could be tested using a more detailed model which implements finite extracellular conductivities and tight extracellular space (Hogues, Leon et al. 1992; Roberts, Stinstra et al. 2008). However, in the modeling study by Hogues et al., while the distance between two adjacent cells was assumed to be constant as 1 nm and their contact area was assumed 10 times larger than that of the flat surface due to the folding, they investigated the efficacy of electric field interactions between two adjacent cardiac cells and concluded that the coupling through the gap junctions is 30 – 130 times more efficient than the coupling through electric field (Hogues, Leon et al. 1992). Therefore, it is unlikely that the tight extracellular space between cells will affect the results of this study. In order to implement the proposed method in experimental setting, it might require a slight modification to the electrode configuration. The proposed method used planar electrodes but these planar electrodes might be unavailable or difficult to implement under experimental conditions. As a result, the planar electrode could be replaced by small number of point electrodes. The stimulus is also applied to the intracellular space and the effect of the extracellular stimulus in this context would need to be studied (Fast, Rohr et al. 1998; Trayanova, Skouibine et al. 1998). In addition to the electrode configuration, only homogeneous tissues were considered and the discrete features of the tissue such as shapes and orientations of cells and distributions of clefts were assumed to relatively uniform throughout. However the monolayer tissue can be cultured with abrupt change in its properties to mimic a diseased state. The proposed method can be readily modified to detect such an abrupt change in the discrete features of the tissue by adding the size and the location as additional model parameters. The proposed method has high computational cost. During the optimization process, the simulation was repeated a few hundred times with different parameters. While a single simulation took for a few hours and the entire optimization took about a week even when using a parallel implementation. Additionally the optimization process sometimes failed converging to the global minimum and the method needed to be restarted with a new initial set of parameters.

There are several methods that could be applied to reduce the long computation time and improve convergence. First, the cardiac tissue model can be built with high order FEM and the size of the linear system to be solved by the simulator can be reduced. The optimization method can also be made more efficient. In this study, the differential evolution (DE) algorithm was used for the estimation. Although DE is quite efficient, the parameters in DE and the error function can be tuned to get a faster and stable convergence.

In this study, the model tissue was assumed as a continuous domain while in previous chapters the tissues were modeled as a discrete one with various cell shapes and orientations. After the conductivities of the continuous tissue model were estimated, the continuous tissue model can be converted to the discrete tissue model by combining information on the discrete features of the tissue. In the discrete tissue model, the EIC is determined by various factors including sizes and orientations of cells, distributions of clefts and gap coupling strength. Sizes and orientations of cells and distributions of gap junctions can be observed from the tissue with a microscope and this information can be used for deciding the corresponding discrete tissue parameters. And then gap coupling strength and intracellular conductivity of a cell can be determined so that the discrete tissue's effective intracellular conductivities are same as those of the continuous tissue.

5. Contributions and Conclusions

In this thesis, I have developed a series of tools to build a discrete cardiac tissue model of neonatal cells in a monolayer to simulate impulse propagation. Moreover, I have tested the methods in several cases and achieved results that were not possible using pre-existing approaches. Chapter 2 described a novel monodomain model to simulate impulse propagation through a tissue whose cells can have arbitrary shapes, orientations and coupling. A 2D finite element method (FEM) model was derived from three dimensional FEM model of a layer of cells by reducing the dimension of the linear system under the assumption of symmetry in the depth direction. Although the derivation of the 2D FEM was straightforward, there were two potential sources of errors when the results from the model were compared to those obtained from the 3D FEM model. First, the reduction process required a single discretization element in the depth direction. This requirement can cause an error in the solution if there is a significant nonlinearity in the intracellular potential. The other potential source of error is due to the gap junction distribution in three dimensional space. While gap junctions can be located anywhere on two dimensional lateral faces of three dimensional cells, the gap junctions for the two dimensional cells can only be located on a one dimensional edge. The 2D FEM was compared to various three dimensional methods with various tissue structures. In addition to this, 2D FEM was compared to 2D finite difference method (2D FDM). In all tests mentioned above, CV and $\dot{V}_{max}$ were compared at various tissue structures and no significant error was found.

In Chapter 3, I presented a method to build a discrete monolayer tissue in which shapes and sizes of cells and distributions of clefts can be controlled. Although the cells in discrete tissue can be generated by using semi-automatic image segmentation schemes, they are difficult to apply to large domains. In addition, it is difficult to use this scheme to create several versions of tissues in which the shapes and sizes of cells and distributions of clefts between cells are treated as random variables. The models are used to study wavefront propagation in a manner similar to that done experimentally, where multiple preparations are tested under the same conditions. Simulations results from the models were compared to the experimental results of Bursac et al.'s showing the relationship of cell orientations and distributions of clefts with CV and anisotropy ratio. As in the experiments, the simulations showed that as the cells oriented transitioned from random to aligned, the longitudinal CV increased and as the transverse directional discontinuity increased by the increase in the amount of clefts, the longitudinal CV decreased (Bursac, Parker et al. 2002).

For the further analysis, two methods were developed to estimate the effective tissue conductivities. In the first method, the membrane elements are removed leaving only an effective network of resistors. The conductivity was evaluated by computing the ratio between mean electric field and total current flux when the current is injected at the one edge of the tissue. This method, termed a global method, cannot be implemented experimentally since the membrane cannot be removed. In the second method, the membrane resistance was estimated from time response of a cell while this cell is stimulated with a long subthreshold pulse. The effective tissue conductivities were found through an optimization process that minimized the difference between the potential patterns from the tissue under the long subthreshold point stimulation and the simulated tissue under the same condition. This method was termed a local method. When the conductivities from the global method and the local method were compared, there were some differences but they had high correlation coefficient (0.97 for longitudinal conductivity, 0.98 for transverse conductivity). The global method showed that Bursac et al.'s experimental results where LCV was decreased when AR > 3.4 (Bursac, Parker et al. 2002) can be explained by the change in effective tissue conductivity in longitudinal direction.

In Chapter 4, the local method to estimate the effective intracellular conductivities was extended to achieve higher accuracy. When the membrane resistance was assumed to be constant, the errors in the estimated effective intracellular conductivities are strongly dependent on the estimated membrane resistance. The estimation method was significantly improved by approximating the membrane resistance as a second order polynomial of membrane potential. The coefficients of this polynomial were estimated with effective intracellular conductivities. The test results using the Pandit model and the Luo-Rudy model showed that this method gives much more accurate estimations compared to the method using a constant membrane resistance.

The methods developed here have advantages and disadvantages compared to *in vitro* studies on engineered monolayers. One advantage is the greater control over tissue properties including cell shapes, orientations, and distributions of gap junctions. The models also allow the ability to monitor individual ionic currents or status of gating variables in the tissue, which is currently not possible experimentally. As a result, the computer model can be used to integrate experimental observations from the molecular to the organ level (Sampson and Henriquez 2005; Silva, Pan et al. 2009). However, the advantages of the model cannot be fully realized if they do not generate behavior that is consistent with that seen in tissues. Experimental studies, while challenging to set up, can provide data in real-time and thus are significantly faster than computer models. For example, simulating 1 msec activity in the domains described in Chapter 4 took about 7 min on a single 2.2 GHz AMD opteron processor and this computational burden increases as the size of tissue increases.

While the methods developed here were found to yield results that were consistent with more traditional methods, the methods still have drawbacks. First, the 2D FEM requires significantly more computer memory when compared to the equivalent continuous model. The memory requirements limit the size of the tissue that can be simulated in practice. It may be possible to only use the discrete cellular structure in regions where it matters. Thus methods will need to be developed to couple the discrete cellular domain with more traditional continuous models. The automatic discrete tissue generation method also requires more works to improve its flexibility. For example, the discrete features of the tissue cannot be changed in the middle of the domain. This would be useful as it is often a case that two or more different types of cells are cultured together in one tissue and these different types of cells have different shapes and orientations. Additionally when the cells orientations are more random, this method produces unintended small holes between cells because the cells were generated from a template cell. All these cases can be improved by using a more sophisticated cell placement method which finds empty space efficiently in the two dimensional space. One approach might be to use quad tree decomposition (Finkel and Bentley 1974). In the current method, a template cell is "pushed" in one direction until the template cell cannot move due to the tissue boundary or the other cells. This approach can make unintended holes depending on the arrangements of cells and the final location of the cell is undetermined until the "pushing" is completed. This makes it difficult to implement a method capable of generating a discrete tissue with variation in cell morphology by the location of the cell. The quad tree decomposition makes it possible to search for empty space in the tissue and the cell can be directly placed in this empty space. This would allow the ability to control the morphology of the cell location by location. In addition, the quad tree decomposition can efficiently find holes in the tissue and these holes can be filled with small cells. Finally the effective tissue conductivity estimation method utilized planar electrodes to stimulate the tissue. The planar electrode is possible but may be difficult to implement experimentally. Thus the planar electrode might need to be replaced with experimentally more suitable electrode configurations and the method would need to be tested.

While the methods can be improved and made faster, they nevertheless open the possibility of studying much more complicated scenarios that are associated with diseased conditions where cells are poorly coupled and the tissue is infiltrated with fibroblasts or nonfunctioning cells. The methods developed in this thesis will allow the ability to investigate the behavior of the discrete cellular networks in critical regimes. Because of the flexibility in creating cellular networks, the simulation can be compared directly to experimental studies using engineered monolayers. Once validated, the models can extended to adult architectures and incorporate the types of heterogeneity in diseased states for which it is not currently possible to develop engineered tissue. Ultimately these models will be used as a testbed to design new experiments to study the role of heterogeneity on arrhythmia and test novel approaches for reengineering the arrhythmogenic substrate either through novel cell therapies or new drugs.

Appendix A

Finite element method implementation for monodomain model

The monodomain model can be expressed in the following form.

$$-\nabla \cdot \sigma_i \nabla V = 0 \qquad \text{in } \Omega \tag{A.1}$$

$$-n \cdot \sigma_i \nabla V = I_m \qquad \text{on } \Gamma \tag{A.2}$$

V is membrane potential, I_m is membrane current, σ_i is intracellular conductivity tensor, Ω is an intracellular space, Γ is a membrane of a cell and n is a normal vector on the membrane, Γ. The membrane current I_m is sum of capacitive, ionic and gap junctional current density, namely

$$I_m = I_{cap} + I_{ion}(V, \boldsymbol{q}) + I_{gap} \tag{A.3}$$

$$I_{cap} = C_m \frac{\partial V}{\partial t} \tag{A.4}$$

$$I_{gap} = g^i_{a,b}\left(V_{i,a} - V_{i,b}\right) \tag{A.5}$$

where I_{cap}, I_{ion}, and I_{gap} are capacitive, ionic and gap junctional current density, respectively. The ionic current is usually expressed as a set of nonlinear differential equations, which are functions of membrane potential and state variables, $\boldsymbol{q}$. The i^{th} gap junctional current between cell a and cell b is a linear function of potential difference between two cells with gap coupling strength parameter $g^i_{a,b}$. This gap junction current provides electrical coupling between cells in the tissue, which is similar to the biological counterpart.

In order to solver the equation (A.1) and (A.2) with FEM, multiplying a proper test function Ψ on both side of equation (A.1) and using integration by part yield following integral identity

$$\int_{\Omega} (\nabla\Psi)^T \cdot \sigma_i \nabla V dx + \int_{\Gamma} I_m \Psi ds = 0 \tag{A.6}$$

After proper discretization of the domain, the equation (A.6) can be written in the matrix-vector format.

$$\begin{aligned} 0 &= A \cdot V^t + B \cdot I_m \\ &= A \cdot V^t + B \cdot \left(C_m \frac{V^t - V^{t-1}}{\Delta t} + I_{ion}(V^{t-1}, \boldsymbol{q}) + G \cdot V^{t-1} \right) \end{aligned} \tag{A.7}$$

where G is a unsymmetrical matrix representing gap coupling strength and the location. In the matrix G, a linear interpolation of membrane potential at discretization nodes is used to get best estimate of the membrane potential at the gap junction when the location of gap junction and the discretization node do not match. Equation (A.7) uses a fully explicit method for the time step integration and it can be rewritten to use Crank-Nicolson method (Keener and Bogar 1998).

$$\begin{aligned} 0 &= \frac{1}{2} A \cdot (V^t + V^{t-1}) \\ &+ B \cdot \left(C_m \frac{V^t - V^{t-1}}{\Delta t} + I_{ion}(V^{t-1}, \boldsymbol{q}) + \frac{1}{2} G \cdot (V^t + V^{t-1}) \right) \end{aligned} \tag{A.8}$$

Rearranging the equation (A.8) gives the following equation.

$$\left(\frac{1}{2}A + \frac{C_m}{\Delta t}B + \frac{1}{2}BG\right)V^t = -\left(\frac{1}{2}A - \frac{C_m}{\Delta t}B + \frac{1}{2}BG\right)V^{t-1} - BI_{ion}\left(V^{t-1}, \boldsymbol{q}\right) \tag{A.9}$$

At $t = 0$, the initial membrane potential and state variable $\boldsymbol{q}$ were plugged in the right hand side of the equation (A.9) and the equation (A.9) is solved to get membrane potential on the left hand side of the equation. This new membrane potential is plugged in the right hand side of the equation again and this process is repeated until the final computation time is reached.

The equation (A.9) was used to implement both continuous and discrete tissue models. For the continuous tissue model, a single large cell was considered as a tissue and proper intracellular conductivities were assigned as the effective tissue conductivities. For the discrete tissue model, when a discrete tissue pattern was provided for the simulation, every pair of cells in this tissue was examined to find adjacent pair of cells. For each neighboring pair of cells, the cell-to-cell contact segment was defined as the cell boundary segment whose distance was closer than 1 μm between the adjacent cells. The gap junction was assumed to exist uniformly on the cell-to-cell contact segment and the potential at the gap junction for the equation (A.5) was obtained by linear interpolation of the membrane potential at the nearest FEM nodes. In implementing the discrete tissue model, the ionic current was assumed not to flow through the lateral faces of the cell throughout the study. The discrete tissue model was compared to the continuous ones and the ionic current through the lateral face causes discrepancy in the membrane surface area between the discrete model and the continuous model. This discrepancy can make the analysis unnecessary complicated.

Appendix B

Optimization process

In Chapter 3 and 4, a nonlinear system optimization was used to estimate model parameters. This optimization process can be described with the Figure A.1. In the first step, the optimization method provides trial values. These trial values were effective tissue conductivities in Chapter 3 and effective tissue conductivities with membrane resistance function parameters in Chapter 4. With these trial values as the model parameters, the tissue simulator simulates the subthreshold response of the tissue. The optimization method requires the creation of an error function that calculates the error between the "measured" data and the simulated data from the simulator. This function is usually defined as a squared sum of the difference between the measured data and the simulated data. In Chapter 3, this subthreshold response was delivered to the optimization error function without additional processing. In Chapter 4, the subthreshold response was spatially averaged to mimic the optical mapping. Based on the output of error function, the optimization method generates next trial values. This optimization process, in which a full simulation is performed at each step, continues until the error is below some user-defined tolerance.

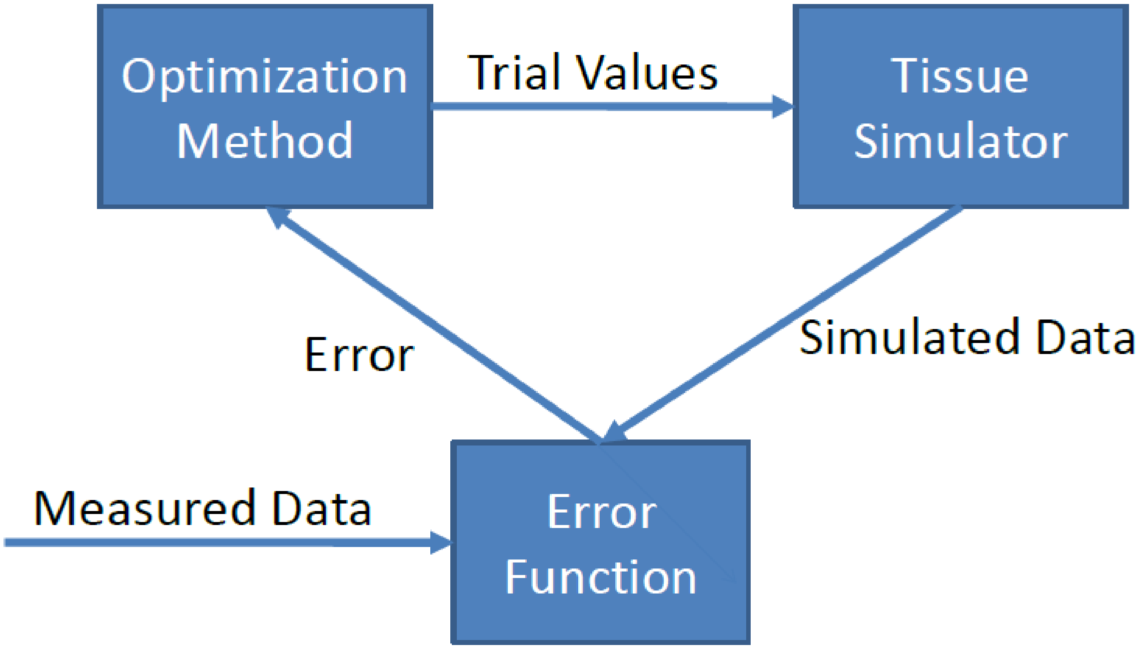

Figure A.1: The optimization process iterates an optimization method, simulator and error function until there is no more improvement in the error.

Differential evolution for global optimization

The optimization method used in this thesis is the differential evolution (DE) algorithm, based on the work of Storn and Price (Storn and Price 1997). DE is a global optimization algorithm, using only a function value but not the derivative of the function. DE is relatively easy to use because it only requires three parameters and has shown a good convergence over wide range of the problems (Storn and Price 1997). Additionally DE is easy to implement for parallel processing, making it suitable for computationally demanding problems.

DE algorithm starts with NP D-dimensional parameter vectors $x_{i,G}, i = 1, 2, \ldots, NP$ while D is the dimensionality of the problem to be optimized. These NP vectors are initial candidates for the optimum solution and selected to cover the entire parameter space. At each generation, new target vectors are generated from the previous generation through mutation, crossover and selection.

1) Mutation: For each target vector, a mutant vector $v_{i,G+1}$ is generated by $v_{i,G+1} = x_{r1,G} + F \cdot \left(x_{r2,G} - x_{r3,G}\right)$. The random index $r1, r2$, and $r3 \in \{1, 2, \ldots, i-1, i+1, \ldots, NP\}$ are randomly selected as mutually different integers. F is a real number between 0 and 2 controlling the amplification of the differential vector $(x_{r2,G} - x_{r3,G})$. In our implementation, F was randomly selected between 0.5 and 1 at every generation (Das, Konar et al. 2005).

2) Crossover: The trial vector $u_{i,G+1}$ is generated from the target vector $x_{i,G}$ and the mutant vector $v_{i,G+1}$ in the following form:

$$u_{i,G+1} = \left(u_{1i,G+1}, u_{2i,G+1}, \dots, u_{Di,G+1}\right) \tag{B.1}$$

$$u_{ji,G+1} = \begin{cases} x_{ji,G} & if\ (random(j) > CR) \quad and \quad j \neq rnbr(i) \\ v_{ji,G} & otherwise \end{cases} \tag{B.2}$$

$$j = 1,2,\dots,D$$

$random(j)$ is uniform random number between 0 and 1 for j^{th} parameter in the i^{th} vector. $rnbr(i)$ is a randomly selected index between 1 and D. $rnbr(i)$ guarantees that the trial vector $u_{i,G+1}$ gets at least one parameter from $v_{i,G+1}$. CR is the crossover constant selected between 0 and 1. CR was 0.9 in our implementation.

3) Selection: The trial vector $u_{i,G+1}$ and the target vector $x_{i,G}$ are compared and the vector producing a smaller cost function value becomes the target vector $x_{i,G+1}$.

The mutation, crossover, and selection step is repeated for a few hundred generations to achieve minimum in the cost function. In our implementation, the number of population NP was 12, the amplification factor F was selected between 0.5 and 1 at each generation (Das, Konar et al. 2005), and the crossover rate CR was 0.9. The algorithm was implemented in parallel by using MPI in C.

References

Ausma, J., M. Wijffels, et al. (1997). "Structural changes of atrial myocardium due to sustained atrial fibrillation in the goat." Circulation **96**(9): 3157-3163.

Bian, W. and L. Tung (2006). "Structure-related initiation of reentry by rapid pacing in monolayers of cardiac cells." Circ Res **98**(4): e29-38.

Briggs, W. L., V. E. Henson, et al. (2000). A Multigrid Tutorial, SIAM.

Bueno-Orovio, A., E. M. Cherry, et al. (2008). "Minimal model for human ventricular action potentials in tissue." Journal of Theoretical Biology **253**(3): 544-560.

Bursac, N., K. K. Parker, et al. (2002). "Cardiomyocyte cultures with controlled macroscopic anisotropy: a model for functional electrophysiological studies of cardiac muscle." Circ Res **91**(12): e45-54.

Cabo, C. and P. A. Boyden (2003). "Electrical remodeling of the epicardial border zone in the canine infarcted heart: a computational analysis." American Journal of Physiology-Heart and Circulatory Physiology **284**(1): H372-H384.

Carmeliet, E. (1999). "Cardiac ionic currents and acute ischemia: From channels to arrhythmias." Physiological Reviews **79**(3): 917-1017.

Cleutjens, J. P. M., W. M. Blankesteijn, et al. (1999). "The infarcted myocardium: Simply dead tissue, or a lively target for therapeutic interventions." Cardiovascular Research **44**(2): 232-241.

Das, S., A. Konar, et al. (2005). "Two improved differential evolution schemes for faster global search." GECCO 2005: Genetic and Evolutionary Computation Conference, Vols 1 and 2: 991-998.

Davis, T. A. and I. S. Duff (1997). "An unsymmetric-pattern multifrontal method for sparse LU factorization." Siam Journal on Matrix Analysis and Applications **18**(1): 140-158.

Entcheva, E., S. N. Lu, et al. (2000). "Contact fluorescence imaging of reentry in monolayers of cultured neonatal rat ventricular myocytes." Journal of Cardiovascular Electrophysiology **11**(6): 665-676.

Everett, T. H. t., H. Li, et al. (2000). "Electrical, morphological, and ultrastructural remodeling and reverse remodeling in a canine model of chronic atrial fibrillation." Circulation **102**(12): 1454-1460.

Fast, V. G. and A. G. Kleber (1993). "Microscopic Conduction in Cultured Strands of Neonatal Rat-Heart Cells Measured with Voltage-Sensitive Dyes." Circulation Research **73**(5): 914-925.

Fast, V. G. and A. G. Kleber (1994). "Anisotropic Conduction in Monolayers of Neonatal Rat-Heart Cells Cultured on Collagen Substrate." Circulation Research **75**(3): 591-595.

Fast, V. G. and A. G. Kleber (1994). "Anisotropic conduction in monolayers of neonatal rat heart cells cultured on collagen substrate." Circ Res **75**(3): 591-595.

Fast, V. G. and A. G. Kleber (1995). "Cardiac Tissue Geometry as a Determinant of Unidirectional Conduction Block - Assessment of Microscopic Excitation Spread by Optical Mapping in Patterned Cell-Cultures and in a Computer-Model." Cardiovascular Research **29**(5): 697-707.

Fast, V. G., S. Rohr, et al. (1998). "Activation of cardiac tissue by extracellular electrical shocks - Formation of 'secondary sources' at intercellular clefts in monolayers of cultured myocytes." Circulation Research **82**(3): 375-385.

Fenton, F. and A. Karma (1998). "Vortex dynamics in three-dimensional continuous myocardium with fiber rotation: Filament instability and fibrillation." Chaos **8**(1): 20-47.

Finkel, R. A. and J. L. Bentley (1974). "Quad trees: A data structure for retrieval on composite keys " Acta Informatica **4**(1): 1-9.

Gardner, P. I., P. C. Ursell, et al. (1985). "Electrophysiologic and Anatomic Basis for Fractionated Electrograms Recorded from Healed Myocardial Infarcts." Circulation **72**(3): 596-611.

Gray, R. A. (1999). "What exactly are optically recorded "action potentials"?" Journal of Cardiovascular Electrophysiology **10**(11): 1463-1466.

Hennan, J. K., R. E. Swillo, et al. (2006). "Rotigaptide (ZP123) prevents spontaneous ventricular arrhythmias and reduces infarct size during myocardial ischemia/reperfusion injury in open-chest dogs." Journal of Pharmacology and Experimental Therapeutics **317**(1): 236-243.

Henriquez, C. S. (1993). "Simulating the electrical behavior of cardiac tissue using the bidomain model." Crit Rev Biomed Eng **21**(1): 1-77.

Henriquez, C. S., A. L. Muzikant, et al. (1996). "Anisotropy, fiber curvature, and bath loading effects on activation in thin and thick cardiac tissue preparations: Simulations in a three-dimensional bidomain model." Journal of Cardiovascular Electrophysiology **7**(5): 424-444.

Hogues, H., L. J. Leon, et al. (1992). "A Model Study of Electric-Field Interactions between Cardiac Myocytes." Ieee Transactions on Biomedical Engineering **39**(12): 1232-1243.

Hubbard, M. L., W. Ying, et al. (2007). "Effect of gap junction distribution on impulse propagation in a monolayer of myocytes: a model study." Europace **9 Suppl 6**: vi20-28.

Jacquemet, V. and C. S. Henriquez (2008). "Loading effect of fibroblast-myocyte coupling on resting potential, impulse propagation, and repolarization: insights from a microstructure model." American Journal of Physiology-Heart and Circulatory Physiology **294**(5): H2040-H2052.

Kanno, S. and J. E. Saffitz (2001). "The role of myocardial gap junctions in electrical conduction and arrhythmogenesis." Cardiovasc Pathol **10**(4): 169-177.

Keener, J. P. and K. Bogar (1998). "A numerical method for the solution of the bidomain equations in cardiac tissue." Chaos **8**(1): 234-241.

Kim, J. M., N. Bursac, et al. (2010). "A Computer Model of Engineered Cardiac Monolayers." Biophysical Journal.

Kostin, S., G. Klein, et al. (2002). "Structural correlate of atrial fibrillation in human patients." Cardiovascular Research **54**(2): 361-379.

Koura, T., M. Hara, et al. (2002). "Anisotropic conduction properties in canine atria analyzed by high-resolution optical mapping - Preferential direction of conduction block changes from longitudinal to transverse with increasing age." Circulation **105**(17): 2092-2098.

Le Guyader, P., F. Trelles, et al. (2001). "Extracellular measurement of anisotropic bidomain myocardial conductivities. I. Theoretical analysis." Annals of Biomedical Engineering **29**(10): 862-877.

Leon, L. J. and F. A. Roberge (1991). "Structural Complexity Effects on Transverse Propagation in a 2-Dimensional Model of Myocardium." Ieee Transactions on Biomedical Engineering **38**(10): 997-1009.

Li, D. S., S. Fareh, et al. (1999). "Promotion of atrial fibrillation by heart failure in dogs - Atrial remodeling of a different sort." Circulation **100**(1): 87-95.

Lin, X. M., C. Zemlin, et al. (2008). "Enhancement of ventricular gap-junction coupling by rotigaptide." Cardiovascular Research **79**(3): 416-426.

Lourakis, M. I. A. (2004). "levmar: Levenberg-Marquardt nonlinear least squares algorithms in C/C++." from http://www.ics.forth.gr/~lourakis/levmar/.

Luo, C. H. and Y. Rudy (1991). "A Model of the Ventricular Cardiac Action-Potential - Depolarization, Repolarization, and Their Interaction." Circulation Research **68**(6): 1501-1526.

Muzikant, A. L., E. W. Hsu, et al. (2002). "Region specific modeling of cardiac muscle: Comparison of simulated and experimental potentials." Annals of Biomedical Engineering **30**(7): 867-883.

Pandit, S. V., R. B. Clark, et al. (2001). "A mathematical model of action potential heterogeneity in adult rat left ventricular myocytes." Biophysical Journal **81**(6): 3029-3051.

Pastore, J. M., S. D. Girouard, et al. (1999). "Mechanism linking T-wave alternans to the genesis of cardiac fibrillation." Circulation **99**(10): 1385-1394.

Pickard, W. F. (1966). "On Propagation of Nervous Impulse down Medullated and Unmedullated Fibers." Journal of Theoretical Biology **11**(1): 30-&.

Plonsey, R. and R. Barr (1982). "The 4-Electrode Resistivity Technique as Applied to Cardiac-Muscle." Ieee Transactions on Biomedical Engineering **29**(7): 541-546.

Plonsey, R. and R. C. Barr (1986). "A Critique of Impedance Measurements in Cardiac Tissue." Annals of Biomedical Engineering **14**(4): 307-322.

Plonsey, R. and R. C. Barr (1987). "Interstitial Potentials and Their Change with Depth into Cardiac Tissue." Biophysical Journal **51**(4): 547-555.

Pollard, A. E. and R. C. Barr (2006). "Cardiac microimpedance measurement in two-dimensional models using multisite interstitial stimulation." American Journal of Physiology-Heart and Circulatory Physiology **290**(5): H1976-H1987.

Qu, Z. (2006). "Critical mass hypothesis revisited: role of dynamical wave stability in spontaneous termination of cardiac fibrillation." Am J Physiol Heart Circ Physiol **290**(1): H255-263.

Roberge, F. A., A. Vinet, et al. (1986). "Reconstruction of Propagated Electrical-Activity with a Two-Dimensional Model of Anisotropic Heart-Muscle." Circulation Research **58**(4): 461-475.

Roberts, S. F., J. G. Stinstra, et al. (2008). "Effect of nonuniform interstitial space properties on impulse propagation: A discrete multidomain model." Biophysical Journal **95**(8): 3724-3737.

Rohr, S., R. Fluckiger-Labrada, et al. (2003). "Photolithographically defined deposition of attachment factors as a versatile method for patterning the growth of different cell types in culture." Pflugers Arch **446**(1): 125-132.

Rose, D. J., H. Shao, et al. (2000). "Discretization of anisotropic convection-diffusion equations, convective M-matrices and their iterative solution." Vlsi Design **10**(4): 485-529.

Rudy, Y. and J. R. Silva (2006). "Computational biology in the study of cardiac ion channels and cell electrophysiology." Quarterly Reviews of Biophysics **39**(1): 57-116.

Sadleir, R. and C. Henriquez (2006). "Estimation of cardiac bidomain parameters from extracellular measurement: Two dimensional study." Annals of Biomedical Engineering **34**(8): 1289-1303.

Sampson, K. J. and C. S. Henriquez (2002). "Interplay of ionic and structural heterogeneity on functional action potential duration gradients: Implications for arrhythmogenesis." Chaos **12**(3): 819-828.

Sampson, K. J. and C. S. Henriquez (2005). "Electrotonic influences on action potential duration dispersion in small hearts: a simulation study." American Journal of Physiology-Heart and Circulatory Physiology **289**(1): H350-H360.

Sharma, V. and L. Tung (2001). "Theoretical and experimental study of sawtooth effect in isolated cardiac cell-pairs." Journal of Cardiovascular Electrophysiology **12**(10): 1164-1173.

Shaw, R. M. and Y. Rudy (1997). "Ionic mechanisms of propagation in cardiac tissue - Roles of the sodium and L-type calcium currents during reduced excitability and decreased gap junction coupling." Circulation Research **81**(5): 727-741.

Shewchuk, J. R. (2002). "Delaunay refinement algorithms for triangular mesh generation." Computational Geometry-Theory and Applications **22**(1-3): 21-74.

Silva, J. R., H. Pan, et al. (2009). "A multiscale model linking ion-channel molecular dynamics and electrostatics to the cardiac action potential." Proc Natl Acad Sci U S A **106**(27): 11102-11106.

Spach, M. S. and J. P. Boineau (1997). "Microfibrosis produces electrical load variations due to loss of side-to-side cell connections: A major mechanism of structural heart disease arrhythmias." Pace-Pacing and Clinical Electrophysiology **20**(2): 397-413.

Spach, M. S. and P. C. Dolber (1986). "Relating Extracellular Potentials and Their Derivatives to Anisotropic Propagation at a Microscopic Level in Human Cardiac-Muscle - Evidence for Electrical Uncoupling of Side-to-Side Fiber-Connections with Increasing Age." Circulation Research **58**(3): 356-371.

Spach, M. S., P. C. Dolber, et al. (1988). "Influence of the Passive Anisotropic Properties on Directional Differences in Propagation Following Modification of the Sodium Conductance in Human Atrial Muscle - a Model of Reentry Based on Anisotropic Discontinuous Propagation." Circulation Research **62**(4): 811-832.

Spach, M. S. and J. F. Heidlage (1995). "The Stochastic Nature of Cardiac Propagation at a Microscopic Level - Electrical Description of Myocardial Architecture and Its Application to Conduction." Circulation Research **76**(3): 366-380.

Spach, M. S., J. F. Heidlage, et al. (2004). "Cell size and communication: role in structural and electrical development and remodeling of the heart." Heart Rhythm **1**(4): 500-515.

Spach, M. S., J. F. Heidlage, et al. (2000). "Electrophysiological effects of remodeling cardiac gap junctions and cell size - Experimental and model studies of normal cardiac growth." Circulation Research **86**(3): 302-311.

Spach, M. S., J. F. Heidlage, et al. (2007). "Mechanism of origin of conduction disturbances in aging human atrial bundles: experimental and model study." Heart Rhythm **4**(2): 175-185.

Spach, M. S., W. T. Miller, et al. (1981). "The Discontinuous Nature of Propagation in Normal Canine Cardiac-Muscle - Evidence for Recurrent Discontinuities of Intracellular Resistance That Affect the Membrane Currents." Circulation Research **48**(1): 39-54.

Storn, R. and K. Price (1997). "Differential evolution - A simple and efficient heuristic for global optimization over continuous spaces." Journal of Global Optimization **11**(4): 341-359.

Trayanova, N., K. Skouibine, et al. (1998). "The role of cardiac tissue structure in defibrillation." Chaos **8**(1): 221-233.

van Oosterom, A., R. W. de Boer, et al. (1979). "Intramural resistivity of cardiac tissue." Med Biol Eng Comput **17**(3): 337-343.

Vandervorst, H. A. (1992). "Bi-Cgstab - a Fast and Smoothly Converging Variant of Bi-Cg for the Solution of Nonsymmetric Linear-Systems." Siam Journal on Scientific and Statistical Computing **13**(2): 631-644.

Vigmond, E. J. and L. J. Leon (1999). "Computationally efficient model for simulating electrical activity in cardiac tissue with fiber rotation." Annals of Biomedical Engineering **27**(2): 160-170.

Wang, L. J. and E. A. Sobie (2008). "Mathematical model of the neonatal mouse ventricular action potential." American Journal of Physiology-Heart and Circulatory Physiology **294**(6): H2565-H2575.

Wang, Y. and Y. Rudy (2000). "Action potential propagation in inhomogeneous cardiac tissue: safety factor considerations and ionic mechanism." American Journal of Physiology-Heart and Circulatory Physiology **278**(4): H1019-H1029.

Ying, W. J. and C. S. Henriquez (2007). "Hybrid finite element method for describing the electrical response of biological cells to applied fields." Ieee Transactions on Biomedical Engineering **54**(4): 611-620.

Zlochiver, S., V. Munoz, et al. (2008). "Electrotonic myofibroblast-to-myocyte coupling increases propensity to reentrant arrhythmias in two-dimensional cardiac monolayers." Biophysical Journal **95**(9): 4469-4480.

Biography

Jongmyeong Kim was born in Keoje, South Korea on November 27th, 1978. He graduated Korea Advanced Institute of Science and Technology with major in electrical engineering and minor in mathematics and earned his B.S. in 2000. After graduation, he worked at Navy for three years as a research engineer. In 2003, he came to U.S. to enroll in the Graduate Program of the Department of Biomedical Engineering at Duke University. He earned his M.S. in 2005 and continued his study in Biomedical Engineering to pursue the Ph.D. at Duke University.

Publications

Navid Pourtaheri, Wenjun Ying, **Jong M. Kim**, and Craig S. Henriquez. Thresholds for transverse stimulation: fiber bundles in a uniform field. *IEEE Transactions on Neural Systems & Rehabilitation Engineering*, 2009. Oct; 17(5): 478-86

Jong M. Kim, Nenad Bursac, and Craig S. Henriquez. A monolayer cardiac tissue model with arbitrary cell shapes. *Biophysical Journal,* 2010. Accepted for publication

Jong M. Kim, Nenad Bursac, and Craig S. Henriquez. Intracellular conductivity and membrane resistance estimation from monolayer cardiac tissue preparation. Manuscript in preparation

Byeong-Yeul Lee, **Jong M. Kim**, Yeunchul Ryu, James R. Connor, and Qing X.Yang. Decreased Callosal Thickness of Patients with Restless Legs Syndrome. Manuscript in preparation